NMR strategies for probing the atomic-level microstructure, dynamics and dopant speciation in metal halide perovskites

Dominik J. Kubicki[a,b], Samuel D. Stranks[a,c], Clare. P. Grey[b]*, Lyndon Emsley[d]**

[a]Cavendish Laboratory, Department of Physics, University of Cambridge, JJ Thomson Avenue, Cambridge, CB3 0HE, UK
[b]Department of Chemistry, University of Cambridge, Lensfield Road, Cambridge, CB2 1EW, UK
[c]Department of Chemical Engineering and Biotechnology, University of Cambridge, Philippa Fawcett Drive, Cambridge, CB3 0AS, UK
[d]Laboratory of Magnetic Resonance, Institute of Chemical Sciences and Engineering, Ecole Polytechnique Fédérale de Lausanne (EPFL), CH−1015 Lausanne, Switzerland

Abstract

Solid-state magic angle spinning NMR is a powerful technique for probing the atomic-level microstructure and structural dynamics in hybrid and all-inorganic metal halide perovskites (MHPs). It can be used to measure dopant incorporation, phase segregation, halide mixing, decomposition pathways, passivation mechanisms, short- and long-range dynamics and other local properties. Here, we review the practical aspects of recording solid-state NMR experiments on halide perovskites that have already enabled unique insight into new compositions, dopants and passivation agents. We discuss the applicability, feasibility and limitations of ^{1}H, ^{13}C, ^{15}N, ^{14}N, ^{133}Cs, ^{87}Rb, ^{39}K, ^{207}Pb, ^{119}Sn, ^{113}Cd, ^{209}Bi, ^{115}In, ^{19}F and ^{2}H NMR in typical experimental scenarios. We highlight the pivotal complementary role of solid-state mechanosynthesis which enables highly sensitive NMR studies by providing large quantities of high-purity materials of arbitrary complexity, and of DFT chemical shift calculations. We examine the broader impact of solid-state NMR on materials research and how seven decades of experience benefit structural studies of halide perovskites. Finally, we summarize some of the open questions in the field of perovskite optoelectronics that could be addressed using solid-state NMR. We thereby hope to stimulate wider use of this technique in the materials and optoelectronics communities.

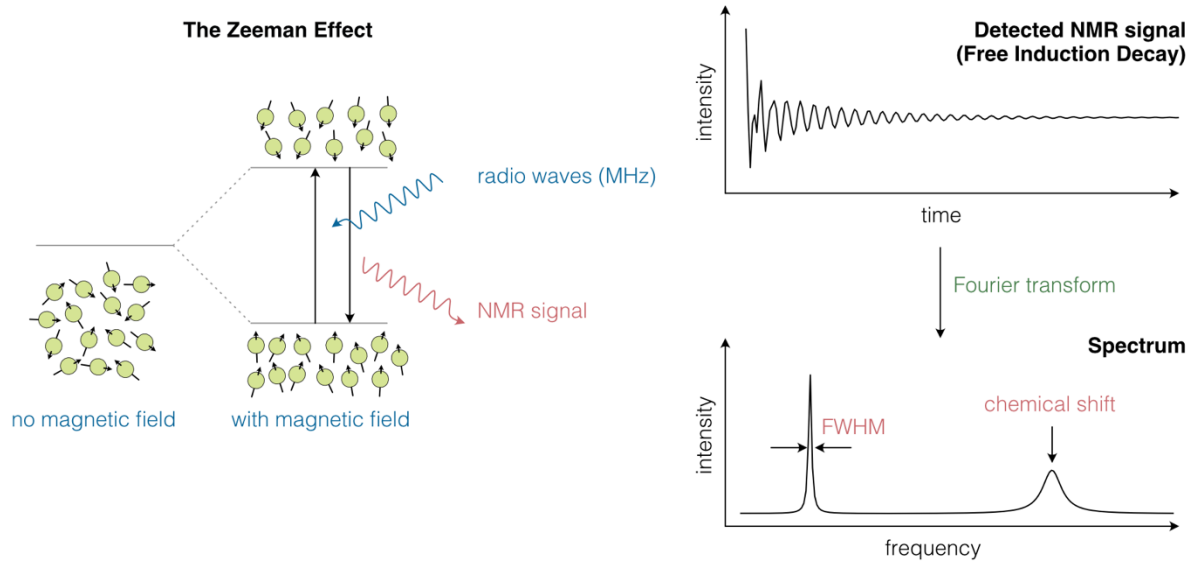

The nuclei of most isotopes in the Periodic Table possess non-zero spin. When an external magnetic field – typically 10-20 T – is applied to a sample containing non-zero spin isotopes, the initially randomly oriented spins align themselves either parallel (lower energy) or anti-parallel (higher energy) relative to the field – this phenomenon is known as the Zeeman effect. This results in the appearance of energy levels, akin to optical spectroscopies, with the corresponding energy required to drive these transitions lying in the radio frequency range of the electromagnetic spectrum. The transitions can be perturbed using short (μs) radio frequency pulses and during the return to equilibrium, they emit radiofrequency waves at the transitions frequencies which can be picked up by a coil in the form of a free induction decay (FID). Fourier transformation of the FID, which is a time-domain signal, yields a spectrum, which represents the signal in the frequency domain. The main features of an NMR signal are its full width at half maximum (FWHM) and position (chemical shift). The unique capability of NMR to study the local structure lies in the fact that the transition frequencies are highly sensitive to the local environment and are therefore affected by the chemical identity and geometrical arrangement of the nearest and next-nearest neighbours as well as the distribution of the electron density in their vicinity, which in turn depend to the electronegativity of the corresponding elements and type of bonding. Since electron densities can be readily calculated using methods of computation chemistry, it is now relatively easy to predict the position of NMR signals in an arbitrary material. The approach linking computational structure prediction, NMR parameter calculation and experimental solid-state NMR is the foundation of a powerful approach to studying the local structure in materials – NMR crystallography. Beyond structural insight, NMR can also be used to access information on dynamics occurring on the timescale between picoseconds and seconds. Dynamics within the structure is what drives the return to equilibrium (relaxation) in NMR experiments. Consequently, relaxation measurements can be used to access the correlation times and activation of energies of the corresponding dynamic processes.

Glossary

Solid-State Nuclear Magnetic Resonance (NMR) – A spectroscopic technique to probe the local environment of nuclei in molecular and extended solids.
Chemical shift – the resonance frequency of a species relative to a frequency standard, usually expressed in parts-per-million (ppm).

Quadrupolar effects – the asymmetric distribution of negative charge around quadrupolar nuclei (i.e. with nuclear spins >1/2) leads to complex line shapes which depend on the extent of asymmetry, making them a powerful tool to study the local electronic environment.
Magic Angle Spinning (MAS) – An experimental protocol in which the solid sample is spun at high rates (typically 10-100 kHz) around an angle of 54.7356° relative to the external magnetic field, leading to substantially improved spectral resolution.
Cross-Polarization (CP) – An experimental protocol allowing the detection of various nuclei with substantially improved sensitivity by transferring to them the intrinsically higher polarisation of nearby ^{1}H (protons).
T_1 (longitudinal) relaxation – The process by which the nuclei return to thermal equilibrium after being perturbed – it determines how fast an NMR experiment can be repeated to acquire more scans and improve the signal-to-noise ratio (SNR). T_1 is usually determined by structural dynamics and paramagnetic dopant concentrations.
T_2 (transverse) relaxation – The process occurring after pulse excitation by which the initially coherent system of nuclear spins loses its phase coherence leading to finite line widths in the NMR spectrum – the longer the T_2 time (i.e. the slower the T_2 relaxation), the narrower the line widths. T_2 is usually determined by structural dynamics and paramagnetic dopant concentrations.
Paramagnetic Relaxation Enhancement (PRE) – the unpaired electrons of paramagnetic species such as transition metal ions can couple strongly to nuclei and cause their rapid T_1 and T_2 relaxation. This effect is distance-dependent and provides a means of studying paramagnetic dopant incorporation into materials.
Nuclear Quadrupole Resonance (NQR) – A spectroscopic technique in which the magnetic resonance signal from quadrupolar nuclei (i.e. with nuclear spins >1/2) is detected in the absence of an external magnetic field. It yields information complementary to NMR and in the case of halogens is often more practical.
Spin-Diffusion (SD) – The process of continuous energy exchange between abundant spins of the same kind (e.g. ^{1}H, ^{19}F) which is driven by dipolar couplings and therefore makes it possible to detect spatial proximities between different species in the NMR spectrum.
Halometalate – any phase containing halides coordinated to a metal cation (e.g. iodoplumbate – $[PbI_6]^{4-}$, bromostannate(IV) – $[SnBr_6]^{2-}$).
Dynamic Nuclear Polarisation (DNP) – a sensitivity-enhancement NMR protocol which allows signal enhancements of a factor of up to ~660, particularly from surfaces, which translate to up to 440 thousand times faster signal acquisition.

1 Introduction

The synthesis and structure of methylammonium lead halide perovskites was first reported in 1978 and their spectroscopic characterization followed shortly afterwards.[1] In 1985, extremely rapid reorientation of methylammonium inside the cubooctahedral perovskite cavity was discovered using solid-state NMR.[2] Subsequent millimeter-wave,[3] IR[4] and more detailed solid-state NMR spectroscopy investigations[5–8] confirmed and further explored the peculiar dynamic behaviour in this class of compounds. Methylammonium tin(II) MHPs were first reported in 1994 and also in this case dynamic disorder of the organic cation was noted.[9] Caesium-based MHPs have been known since much earlier, with the first report of $CsSnI_3$ in 1925[10] and of the black perovskite $CsPbI_3$ in 1959.[11]
A renaissance of interest in MHPs followed the 2009 report and the two subsequent works which reported MHPs used as visible-light sensitizers for photovoltaic solar cells based on mesoporous TiO_2.[12–14] A

number of features have contributed to the subsequent success of MHPs in optoelectronics: facile solution synthesis, optoelectronic properties being largely immune to lattice defects, long photogenerated charge carrier lifetimes, and compositional tunability, to name a few. The power conversion efficiency of perovskite solar cells has risen from 3.8% to over 25% within a decade.[12,15] Considerable advances in MHP-based light emitting devices, including light-emitting diodes (LEDs) and lasers, have also been made in recent years.[16,17]

The generic stoichiometry of MHPs can be represented as ABX_3, where *A* is a small cation such as methylammonium, ($CH_3NH_3^+$, MA), formamidinium ($CH_3(NH_2)_2^+$, FA), caesium, or their mixture. The inorganic sublattice is formed by $[BX_6]^{4-}$ octahedra, where *B* is a divalent metal (Pb^{2+}, Sn^{2+}, Ge^{2+}) or their mixture while *X* is a halide: I^-, Br^- or Cl^-, or their mixture (**Figure 1**). A closely related group of materials with a mixture of divalent and trivalent metal ions (e.g. Ag^+ and In^{3+}) on the B site is known as double perovskites (or elpasolites) with the general formula of $A_2B'B''X_6$. We also note that the term "perovskite" is currently used to designate a large number of halometalate phases with various stoichiometries loosely related to the phase prototype structure of $CaTiO_3$, e.g. Ruddlesden-Popper and Dion-Jacobson phases (referred to as layered perovskites) or antifluorites (referred to as vacancy-ordered perovskites). The most efficient perovskite solar cells today are based on complex mixtures of A-site cations, halides and the compositions are typically doped with small organic molecules or inorganic dopants to further improve their optoelectronic performance.[18] Until very recently, the atomic-level mechanism of action of different dopants was largely hypothetical since there were no protocols to probe their structure at the atomic level in complex perovskite formulations.

To fill this important gap, we and others have developed a range of solid-state NMR experimental approaches which make it possible to investigate phenomena such as A-, and B- cation mixing,[19–25] phase segregation resulting from doping with ions which do not incorporate into the perovskite structure,[22,26,27] halide mixing,[28–31] interfacial passivation mechanisms,[32–35] ambient degradation mechanisms,[31,36] and cation and anion dynamics.[6,37–40,40–42] Some aspects of solid-state NMR of MHPs have been recently reviewed.[43,44] Here, we provide a broad overview of progress so far, we focus on practical aspects of applying solid-state NMR to MHPs and point to the areas where it has the potential to provide new unparalleled information.

The rapid advance of solid-state NMR for MHPs has been largely possible due to the advent of their solid-state mechanosynthesis,[45–48] yielding large quantities of crystalline material (>1000 mg) of any desired composition with no use of solvents. We have demonstrated this by preparing large libraries of hybrid and all-inorganic mixed-cation (Cs, MA, FA) and mixed-halide lead and tin[31] materials doped with small organic cations,[33,35,49] alkali and alkaline earth[19,26,27] and transition[21,22] metals. Other groups have demonstrated the applicability of mechanosynthesis to mixed-halide systems and found optimal experimental conditions to prepare pure-phase all-inorganic perovskite phases with different dimensionalities,[29,30,50–52] including MHP nanocrystals.[53,54] An alternative approach to obtaining bulk solid perovskite samples is to use solution[55] of high-temperature melt[56] synthesis. Smaller amounts can be obtained by using thin film material scraped off of glass substrates after spin coating. The use of mass-limited thin film samples is feasible and straightforward for ^1H,[32] and has been demonstrated for ^{13}C, ^{133}Cs and ^{14}N, although at the price of long acquisition times (>12 hours).[19,20] The advent of sensitivity-enhanced detection protocols made acquisition of ^{207}Pb spectra on thin films of MHPs possible.[57]

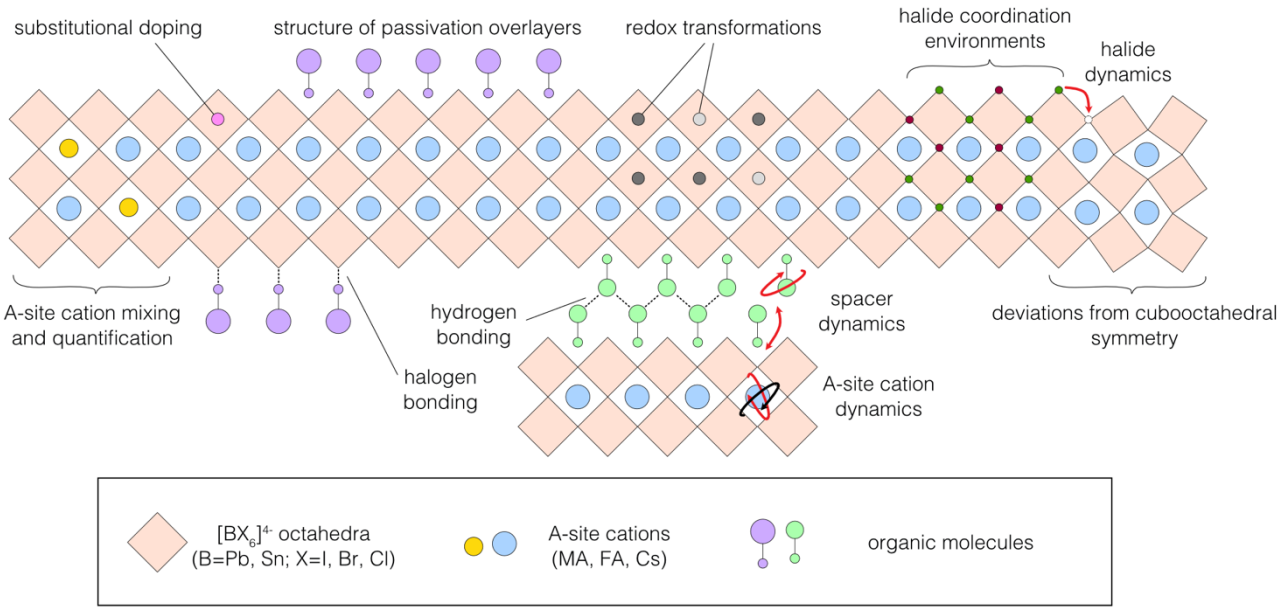

Figure 1. Challenges related to studying of structure and dynamics in MHPs materials. Solid-state NMR is perfectly placed to address component mixing, chemical transformations, elucidate binding modes, coordination environments and structural dynamics.

In what follows, we describe the experimental strategies developed so far through specific examples that highlight the information content provided by solid-state NMR and by detailing the rich science that has ensued (**Figure 1**). The review is structured as follows: we first give a brief overview of the current position of solid-state NMR in materials research in general (section 2), discuss how this decades-long experience translates to its emerging applications in MHP research specifically (section 3) and give an overview of the approaches developed to date (section 4). We first focus on the protocols developed for A-site cations (section 5) and additives that do not incorporate into MHPs (section 6). We then move on to B-site cation dopants in lead MHPs and how ^{207}Pb NMR specifically can be used to study the halide composition (section 7). In section 8, we describe the use of ^{119}Sn to study halide coordination and redox transformations in tin MHPs. In section 9, we discuss the progress made in solid-state NMR of MHPs based on silver, indium and bismuth. Section 10 is devoted to the effects of doping on the symmetry of the A-site cation cage, as probed by ^{14}N. In section 11 we summarize the studies of structural dynamics in MHPs by ^{2}H and ^{14}N NMR. We close by discussing some of the open questions, challenges and milestones where solid-state NMR can provide substantial insight.

2 Solid-state NMR as a general tool for studying the local structure and dynamics of solid materials

Since its discovery in 1946,[58,59] NMR of solids has been extensively used to study solid materials[60] such as natural[61,62] and synthetic[63] polymers, oxide and non-oxide inorganics,[64–66] glasses,[67,68] zeolites,[69–71] metal-organic frameworks,[72–74] cements,[75–77] battery materials,[78–80] semi-[81] and superconductors[82–84], metals and their alloys[64] as well as nanostructures[85,86]. The key technological and conceptual breakthroughs which allowed its widespread use in materials research include the development of magic angle spinning to increase spectral resolution,[87] cross-polarization (CP) to increase sensitivity,[88] two-dimensional NMR to allow homo- and heteronuclear correlation experiments,[89] tracing atom connectivity[90] and measuring internuclear distances[91]. More recently, the key challenge of high-resolution solid-state NMR, namely its comparatively low sensitivity, has been addressed by the advent of Magic Angle Spinning (MAS) Dynamic Nuclear Polarisation (DNP)[92,93] and in particular the impregnation methods for surface enhancement in

materials.[94] MAS DNP has allowed surface-sensitive studies in porous and structural materials, polymers, nanoparticles, pharmaceuticals, and biomolecular structures, that up till then had been out of reach. DNP also considerably increases NMR detection sensitivity in the bulk of materials where the high polarization is carried from the surface into the bulk by spin diffusion. This process is general and has been demonstrated in both protonated[95] and proton-free solids[96]. The application of solid-state NMR to determine the structure of solids in combination with computational and diffraction-based strategies has been reviewed in a comprehensive monography on NMR crystallography.[97]

The versatility of solid-state NMR in providing structural information is best illustrated by a selection of recent problems in materials research where it has been instrumental to establishing structure-property relationships. In the context of battery research, ^{1}H and ^{7}Li MAS NMR have allowed to unambiguously establish the charge-discharge mechanism in an air-lithium battery endowed with unprecedented stability and performance owing to the addition of LiI.[78] In heterogeneous catalysis, solid-state NMR has recently allowed to determine the atomic-level structure of active sites in a variety of catalysts. For example, ^{13}C-^{15}N and ^{29}Si-^{15}N NMR distance measurements have been used to provide local structural constraints to determine the three-dimensional structure of an organoplatinum complex grafted on amorphous silica with a precision of 0.7 Å.[98] In 2016, hexagonal boron nitride (*h*-BN) was demonstrated as a highly efficient and selective catalyst of oxidative dehydrogenation alkanes to olefins,[99] and the atomic-level structure of the catalytically active sites has been subsequently established using ^{11}B and ^{14}N solid-state NMR.[100,101] ^{13}C and ^{15}N MAS NMR experiments have been used to establish the molecular mechanism of CO_2 chemisorption in a large library of amine-functionalised MOFs intended for carbon-capture applications.[102] Finally, ^{1}H and ^{29}Si solid-state NMR has recently resolved one of the most long-standing debates in the chemistry of cement by providing an atomic-level three-dimensional picture of the calcium silicate hydrate (C-S-H) phase, the main binder of concrete.[76]

Computation of NMR parameters has been an essential component to the success of solid-state NMR in materials research. Not only does it provide a way to predict, assign and interpret experimental data, but it also allows to test structural models within the powerful framework of NMR crystallography.[103–105] Unlike diffraction-based methods, NMR directly probes the local atomic environment and therefore does not rely on the presence of long-range order. The advent of accurate DFT methods to calculate chemical shifts and quadrupolar parameters, in particular based on the Gauge Including Projector Augmented Wave (GIPAW) approach[106–108] has enabled crystallographic elucidation of the local structure in highly disordered and amorphous solids such as glasses and ceramics but also polymorphs of pharmaceuticals, molecular crystals and extended solids.[97] Molecular dynamics (MD) has been employed to account for subtle effects observed in NMR shifts and relaxation parameters induced by fast small-amplitude motions.[109] More recently, machine-learning approaches have been proposed to aid rapid and accurate calculation of NMR parameters.[110,111] The great potential of combining solid-state NMR distance measurements with MD simulations has been showcased in a study elucidating the mesoscale spatial apportionment of functional groups in a series of mixed-linker MOFs, wherein the linkers have been shown to distribute in a random, alternating or clustered manner, depending on their functionalities and ratios.[72]

Studies of dynamics are a particularly prominent area of solid-state NMR research owing to its unique capacity to probe timescales across over 12 orders of magnitude, corresponding to correlation times, τ_C, between picoseconds and seconds. Different timescales can be accessed using different NMR experiments, typically carried out as a function of temperature. Slow dynamics ($\tau_C \sim$ seconds) is typically related to changes in the conformation of molecules, diffusion of species and reorientation of long chains in solid polymers. Since different orientations or sites are characterised by different NMR chemical shifts, their interconversion can be probes using exchange spectroscopy (EXSY) experiments. Typical examples include the use of EXSY to study diffusion of lithium in ceramics[112] and cathode materials[113], gas diffusion

in zeolites[114], and side-group flips and chain rearrangements in polymers[115]. Intermediate dynamics (τ_C ~ ms-μs) occurs on the same timescale as the FID acquisition (i.e. comparable to T_2 relaxation) and therefore may strongly affect the line shape. A classic example of this is deuterium NMR,[116] which has been used to study dynamics in, for example, organic molecules adsorbed in porous coordination polymers,[117] MOF linkers,[118,119] and glassy solids[120]. Fast dynamics (τ_C ~ μs-ps) occurs on a timescale comparable with the inverse of the NMR resonance frequency (tens to hundreds of MHz) and as a consequence affects spin-lattice T_1 relaxation. A large number of works have been carried out to study fast ion dynamics in amorphous solids and glasses,[121] as well as lithium transport across numerous classes of inorganic materials relevant to energy storage[122].

A slightly more exotic way of studying ion diffusion *via* relaxation uses short-lived highly spin-polarised (80-100%) β-emitters: radionuclides (β-NMR) or muons (muon spin resonance – μSR) implanted within the solid. Their β-decay violates parity conservation, hence the resulting β particle (electron or positron) is emitted preferentially along the direction of the radionuclide/muon spin. Spin-lattice relaxation decreases the polarisation of the β-active nuclei or muons leading to radiation asymmetry, which is a direct measure of the polarisation changes over time and reflects ion dynamics in the solid. Muon spectroscopy has recently emerged as powerful tool to study ion diffusion in battery materials.[123] The use of β-NMR to study nanocrystalline and amorphous materials has been reviewed.[124]

3 Standing on the shoulders of giants – seven decades of solid-state NMR research as the source of inspiration for studying MHPs

In the context of MHP research, the tremendous amount of previous solid-state NMR research on materials is important for several reasons. Firstly, most of the experimental approaches developed for other materials can be applied to MPHs directly. For example, MAS is the principal way in which high-resolution NMR spectra are recorded today. Further, a variety of previously developed pulse sequences can used to obtain a comprehensive atomic-level picture of a new material: starting from simple one-dimensional spectra (Hahn echo, CP) to more advanced correlation experiments evidencing through-space (HETCOR, recoupling sequences) and through-bond (INADEQUATE, J-HMQC) proximity between nuclei, quantitative distance measurements (REDOR and its variants), to studying dynamics *via* relaxation measurements.

Secondly, composites containing MHPs and other solid components have paramount importance in practical applications. Since those additional components in their pure form have been thoroughly characterised by solid-state NMR before, it is now possible to use that knowledge to analyse how their local structure is affected in composites with MHPs. For example, optoelectronic devices frequently interface PEDOT:PSS (a hole transport layer) and MHPs or use macromolecular additives such as PVP,[125] PEG,[126] PMMA,[127] or polycarbonates.[128] A number of recent works have reported MHP-MOF hybrids with emergent properties[129] as well as MHP-zeolite[130] and MHP-glass[131] composites acting as a stable encapsulation for the photoactive material. The atomic-level structure of the interface between the MHPs and the various polymers, and inorganic/hybrid matrices is yet to be uncovered. When MHPs are deposited on glass, spontaneous diffusion of ions can change the structure of both materials although this phenomenon also has not yet been characterised at the atomic level.[132] A proof-of-concept photobattery based on a 2D MHP capable of both generating and storing energy via reaction with lithium, however the structural changes so far have only been studied using X-ray diffraction.[133] These selected examples show the ample potential high-resolution solid-state NMR has in the field of broadly understood MHP optoelectronics.

Finally, in the context of MHP research, coupling solid-state NMR experiments with DFT calculations of NMR parameters has allowed us and others to corroborate speciation of various additives by predicting their chemical shift and quadrupolar parameters in different structural scenarios, e.g. that of hypothetical incorporation into the MHP structure.[19,24,26,134] For example, the NMR crystallography

approach allowed us to identify different binding modes of small organic molecules interacting with MHP surfaces via halogen bonding,[135] while MD enabled us to qualitatively interpret dynamics-induced effects in CP spectra of MHPs featuring labile hydrogen bonding networks[33] as well as rationalize the role of SCN^- in aiding the formation and stabilization of α-$FAPbI_3$.[136]

4 Applicability of solid-state NMR to components present in MHPs

Table 1 shows a rundown of the nuclei relevant to current MHP materials research. It summarizes the main structural/dynamic information yielded by each of the nuclei, typical experiment times as well as key experimental considerations.

Table 1. Main solid-state NMR strategies developed for halide perovskite research to date.

Nucleus	main information content	typical measurement times*	key experimental considerations	ref.
		A-site cations, dopants, molecular modulators		
^{1}H	A-site cation quantification, connectivity between perovskite and organic dopants	seconds-minutes	A-site cations well resolved due to nearly isotropic motion, organic cations in 2D/3D materials well-resolved due to comparatively small dipolar interactions in halometalates	23,32,37,137
^{13}C, ^{15}N	phase composition, local structure of A-site cations and organic dopants	minutes (100 K) hours-days (RT)	low-temperature (100 K) measurements considerably more sensitive	20,37,49
^{133}Cs	caesium speciation	minutes (bulk phases), hours (dopants, thin films)	highly sensitive, relatively slow relaxation, feasible even for submilligram sample quantities	19,21,30,138,139
		Additives		
^{87}Rb	rubidium speciation	seconds (bulk phases) minutes/hours (additives)	highly sensitive, fast relaxation, feasible for submilligram sample quantities	19
^{39}K	potassium speciation	minutes (bulk phases) hours/days (additives)	moderately sensitive, high (>10 T) magnetic fields preferable, only bulk sample measurements are viable	19,26
		B-site cations		
^{207}Pb	halide coordination environments of lead sites, presence of PbI_2, degradation products, halide dynamics	minutes (single halides), hours (mixed halides)	sensitivity-enhanced techniques available (<1h measurement times for <20 mg of material), indirect probe of A-site cation composition	28–30,36,42,57,140
^{119}Sn	halide coordination environments of tin sites, A-site cation composition, degradation products, halide dynamics	minutes (for T_1<1 s), hours (for T_1>1 s)	T_1 very sensitive to composition (see Figure 2b). Very sensitive to tin oxidation state. Pure tin(II) halostannates give extremely broad spectra unless prepared under reducing conditions.	31
^{209}Bi, ^{115}In	B-site cation mixing in Ag/Bi/In double MHPs	minutes	B-site cation mixing (Bi^{3+}/In^{3+}) leads to very broad signals due to sizable quadrupolar broadening.	24
		Probes of dynamics		
^{14}N	very sensitive to cubooctahedral symmetry, A-site cation dynamics	minutes (highly symmetric phases), hours (lower than cubooctahedral symmetry)	most straightforward in 3D perovskites (nearly isotropic A-site cation reorientation in highly symmetric local environment), useful for studying phase transitions	structure: 20,37,49,141 dynamics: 6,37–40
^{2}H	dynamics of A-site cations and organic additives	seconds/minutes	requires isotopic labelling (e.g. by $NH_3^+ \rightarrow ND_3^+$ exchange with heavy water)	6,20,37,49 42
μ^+	A-site and halide dynamics	hours	requires a large amount of material (~1 g) and a pulsed muon source	142,143

*on bulk (50-100 mg) samples. Measurement times on thin films (1-5 mg) need to be substantially longer.

Besides yielding structural information, ^{1}H, ^{207}Pb, ^{13}C and ^{15}N NMR have also been used to study dynamic processes in $MAPbI_3$.[40,144] ^{19}F MAS NMR has been used to evidence the interaction of microcrystalline $FA_{0.85}MA_{0.15}PbI_{2.55}Br_{0.45}$ with a fluorine-containing molybdenum complex,[145] study the atomic-level interaction between MHPs and a passivation agent capable of engaging in halogen bonding,[135] and the speciation of BF_4^- in $MAPbI_3$.[146] As the use of fluorine-containing doping agents becomes more widespread, the field will likely see more solid-state NMR studies employing ^{19}F MAS NMR. The local structure of other halogens has been studied using $^{35/37}Cl$, $^{79/81}Br$ and ^{127}I NMR and NQR measurements and the subject has been recently thoroughly analysed in a recent review in the context of micro- and nanocrystalline MHPs.[147–150]

One of the key experimental considerations in multi-nuclear solid-state NMR is the choice of optimal experimental parameters so as to maximize the signal-to-noise ratio (SNR) during the accessible measurement time window. The recycle delay, which is adjusted based on the longitudinal relaxation time, T_1, may span up to 6 orders of magnitude, depending on the nucleus and temperature. **Figure 2** shows typical T_1 values for nuclei pertinent to MHPs research. Notably, ^{133}Cs is characterized by relatively long relaxation times, typically in excess of 100 s. Relaxation times well below 1 s (^{207}Pb, ^{14}N, ^{2}H), contribute to the ease of detection due to the faster possible scan repetition rates. As a rule of thumb, optimal SNR per unit time is obtained when the recycle delay is set to $1.3\cdot T_1$, while quantitative results require $5\cdot T_1$. Quantification is straightforward for most nuclei and acquisition schemes, but it is important to point out that the most efficient way of obtaining ^{13}C and ^{15}N data, *i.e.* through ^{1}H-^{13}C and ^{1}H-^{15}N cross-polarization (CP), is generally not quantitative. There exist well-established experimental schemes to make CP quantitative,[151] although this has not yet been applied specifically to MHPs.

Tin MHPs are particularly noteworthy since ^{119}Sn relaxation times depend very strongly on the halide composition and dimensionality of the structure (**Figure 2b**). For example, quantitative detection of coexisting $MASnCl_3$ (T_1=60 s) and metallic tin (T_1=0.1 ms) would require a recycle delay of 300 s which corresponds to $5\cdot T_1$ for $MASnCl_3$ and $3000000\cdot T_1$ for β-Sn.[31]

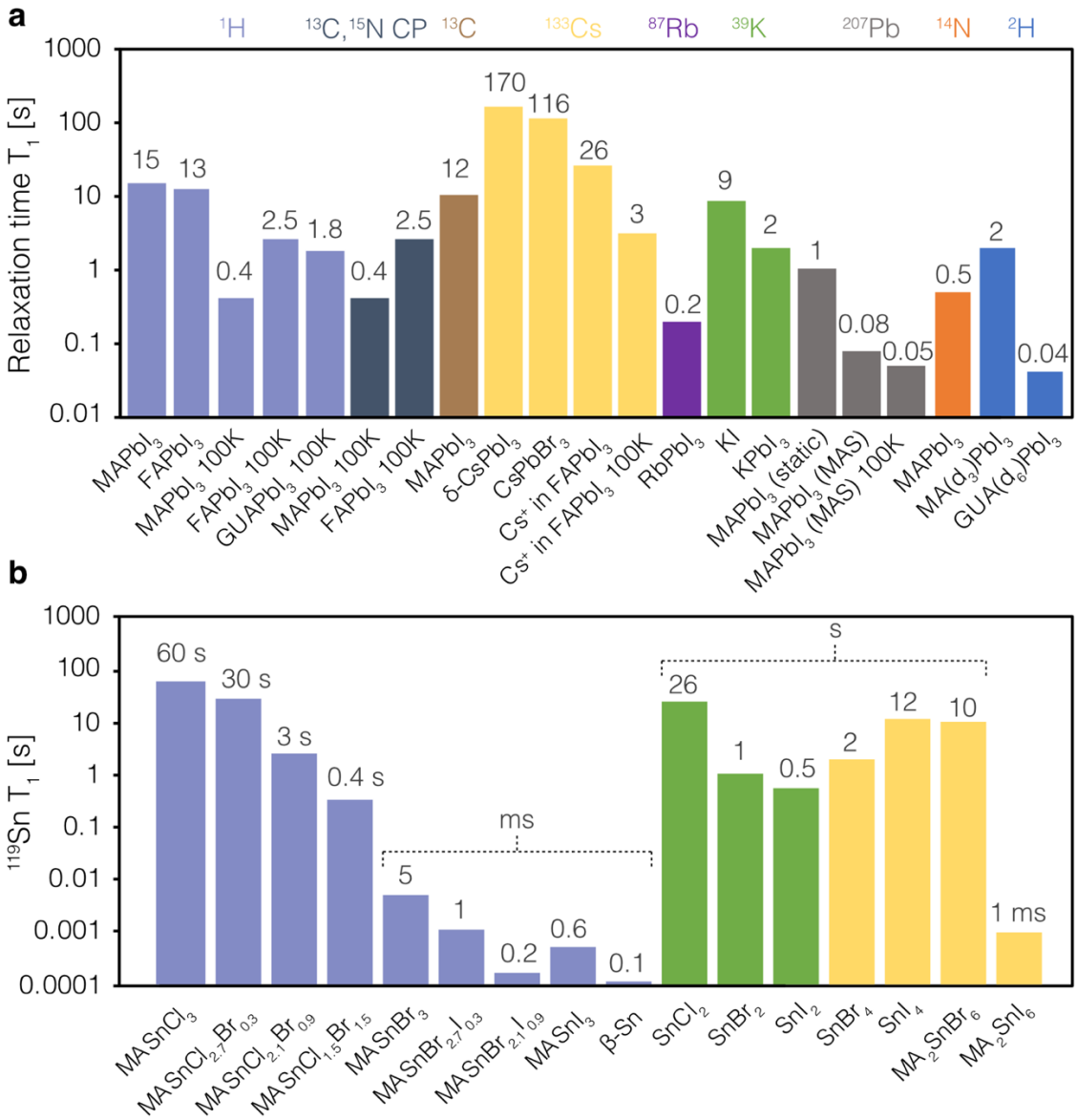

Figure 2. **Typical longitudinal relaxation times, T_1, reported in the literature for different nuclei pertinent to MHPs.** (a) Various nuclei in lead MHPs and related phases, (b) ^{119}Sn in halides and halostannates. In general, T_1 depends slightly on the magnetic field strength. The data collected here were recorded between 10 and 21 T and at room temperature under MAS unless noted otherwise. Further experimental details can be found in the respective reports referenced in the text. Adapted with permission.[31] 2020, American Chemical Society.

5 A-site cation composition

5.1 Quantification of MA/FA: ^{1}H MAS NMR

Solid-state ^{1}H (proton) NMR spectra of organic solids are typically broad and featureless due to the presence of strong ^{1}H-^{1}H dipole-dipole couplings. Satisfactory resolution can be obtained by applying dipolar decoupling sequences[152–155] or very fast magic angle spinning (MAS)[156,157], which leads to partial averaging of the dipolar couplings. In comparison, solid-state ^{1}H spectra of MHPs are exceptionally well-resolved and more closely resemble liquid-state NMR spectra. The dipolar broadening is determined by the strength of dipolar coupling which is proportional to the inverse cube of the internuclear distance. While typical proton-dense organic solids contain a continuous network of ^{1}H-^{1}H contacts below 2 Å, the organic A-site cations in MHPs are separated by ~6 Å. More importantly, the A-site cation is reorienting nearly

isotropically on the picosecond timescale,[6] which acts to very significantly reduce the effective dipolar coupling strength. This feature allows quantification of organic components in MHPs using commonly available MAS probes and moderate sample spinning rates (10-20 kHz). For example, ^{1}H MAS NMR has been used to quantify the MA/FA ratio in bulk microcrystalline powders[37,137,158] and thin films[32,136], quantify the amount of organic passivation dopants,[32] to show that MA is not appreciably volatile during prolonged 150 °C annealing of Cs/MA/FA thin films,[32] and to monitor humidity-induced degradation of $MAPbI_3$.[159] A major advantage of ^{1}H MAS NMR is its superior sensitivity which makes it amenable to studies on mass-limited (<1 mg) thin film samples. We have found that scraping the material off of ten 2.5×1.5 cm glass substrates spin-coated with MHPs using the conventional antisolvent process[160] leads to 1-2 mg of material which is sufficient for the detection of high signal-to-noise ratio (SNR) ^{1}H MAS NMR data. Since ^{1}H spectra typically only span a range of about 15 ppm, an important consideration in ^{1}H MAS NMR is whether the different organic species can be resolved in the one-dimensional spectrum (**Figure 3a**). For example, MA and FA have chemical shifts which are sufficiently different to be fully resolved while for ethylammonium (EA) and MA, the NH_3^+ peaks overlap entirely but sufficient resolution is obtained for the CH_3 and CH_2 groups.

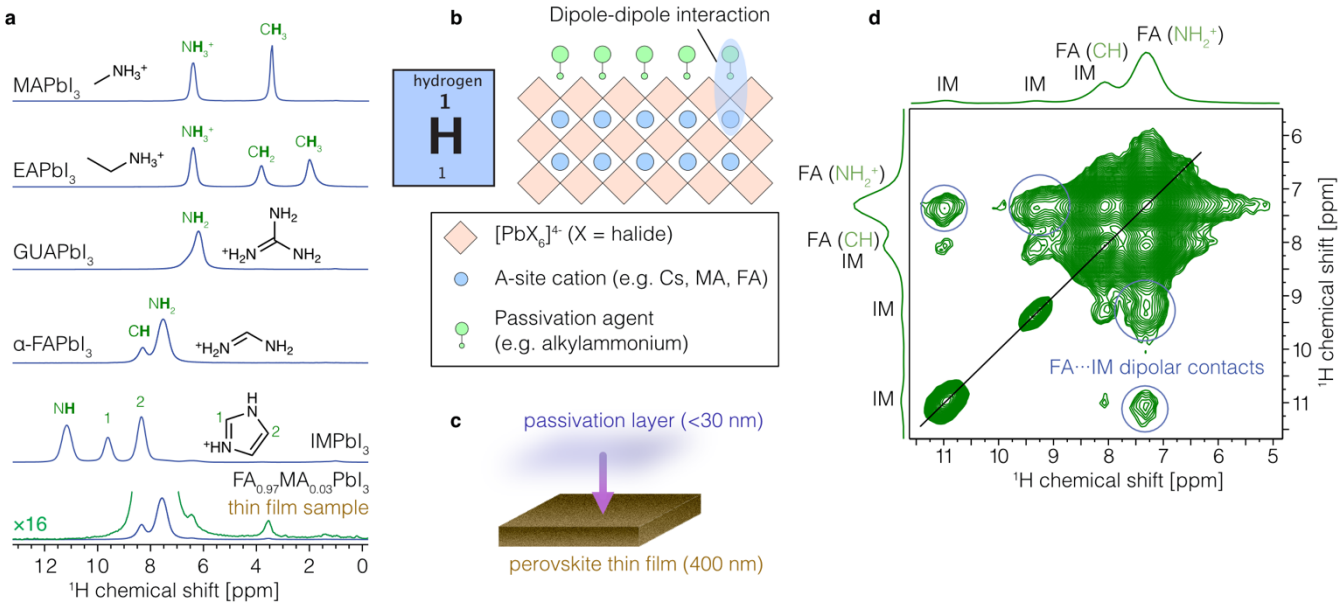

Figure 3. Identification, quantification and proximity of organic cations in MHPs from ^{1}H solid-state NMR. (a) ^{1}H MAS NMR spectra of iodoplumbate phases at 21.1 T, 20 kHz MAS and 298 K: $MAPbI_3$, $EAPbI_3$ (EA – ethylammonium), $GUAPbI_3$ (GUA – guanidinium), α-$FAPbI_3$, $IMPbI_3$ (IM – imidazolium), $FA_{0.97}MA_{0.03}PbI_3$ (thin film, annealed at 150 °C for 30 minutes, quantitative). The spectrum shows that MA is quantitatively preserved in the composition despite prolonged high-temperature annealing. Adapted with permission,[32] 2019, Nature Publishing Group. (b) A schematic representation of a perovskite lattice interacting with a small organic passivation agent. (c) Typical thickness of the perovskite and passivation layer in MHP solar cells. (d) ^{1}H-^{1}H spin-diffusion measurement evidencing atomic-level proximities in a MHP thin film surface-passivated with imidazolium (IM). Adapted with permission.[32] 2019, Nature Publishing Group.

5.2 Atomic-level passivation mechanisms: two-dimensional ^{1}H-^{1}H and ^{19}F-^{19}F spin-diffusion

One of the strategies developed to improve the performance and stability of MHP thin films relies on the deposition of a thin overlayer containing organic molecules, which have been speculated to bind to the MHP layer and thereby remove some of the defects relevant to non-radiative recombination processes. This

protocol is referred to as surface passivation and until recently its microscopic mechanism has been unknown. The presence of dipolar coupling in the solid-state allows ^{1}H spins to communicate *via* magnetization exchange (spin diffusion, SD) making it possible to evidence spatial proximities between different groups of atoms, inter- and intramolecularly, in two-dimensional ^{1}H-^{1}H SD experiments.[161,162] The presence of off-diagonal cross-peaks linking groups of protons belonging to different molecules (indicated by blue circles in **Figure 3d**) is proof of their atomic-level spatial proximity. The length scale can be determined on the 10 Å - 100 nm range (depending on how the experiment is set up). We have used this approach to show the formation of physically attached 1D passivation layers of ethylammonium, guanidinium and imidazolium lead iodide on the surface of a 3D perovskite thin film (**Figure 3b-d**),[32] the formation of layered haloplumbates with adamantly-based spacers,[49] as well as mixed FA/5-ammoniumvaleric acid[33] and FA/MA[136] haloplumbate phases directly responsible for the stabilisation of the black perovskite phase of $FAPbI_3$. This approach also been applied to $MAPbI_3$ passivated with tetrapropylammonium iodide.[163] In the same vein, we have used ^{19}F-^{19}F experiments to study cross-talk between different binding modes of a fluorine-containing perovskite passivation agent.[135] The study of SD dynamics is one of the cornerstones of NMR crystallography of organic solids.[164,165] Its use for providing structural constraints in MHPs and in particular disordered passivation layers is an exciting but as yet unexplored avenue.

5.3 Sensitive detection of A-site cations: low-temperature cross-polarisation

The organic components of MHPs can be detected using ^{13}C MAS NMR and their chemical shifts are sensitive probes of the local structure, allowing one to evidence the formation of new species, non-covalent interactions, and provide information on order and disorder. There are two main strategies for obtaining ^{13}C spectra in the solid state: direct excitation and the use of cross-polarization (CP)[166]. The latter scheme uses the comparatively high Boltzmann polarization of protons which is transferred to ^{13}C, thereby enhancing its detection sensitivity by a factor of up to 4. In addition, in CP, the recycle delay is determined by the relaxation of protons, which is often faster than that of ^{13}C, making signal averaging faster. However, CP transfer relies on ^{1}H-^{13}C dipolar couplings which are largely suppressed by the fast reorientation of the A-site cation, rendering CP inefficient at room temperature (RT). This limitation can be overcome by using cryogenic temperatures (~100 K) to suppress the isotropic motion and restore the C-H dipolar couplings, thereby rendering ^{1}H-^{13}C CP efficient (**Figure 4a**). Cryo-NMR has the added benefit of intrinsically higher thermal polarization at 100 K, boosting sensitivity by an additional factor of ~3 with respect to RT, and shortening of ^{1}H relaxation times in MHPs (e.g. 15 s at RT vs. 0.4 s at 100 K for $MAPbI_3$, **Figure 2a**) allowing faster signal averaging. For example, we have shown that high SNR ^{1}H-^{13}C CP MAS spectra can be detected on a variety of hybrid haloplumbates in a matter of minutes for ~70 mg of material, which is an amount readily obtainable by mechanosynthesis or spin casting (**Figure 4a**).[20,37,49] ^{1}H-^{13}C CP MAS cryo-NMR spectra are highly sensitive to phase composition, with significant shifts for as little as 5 mol% organic cation doping (**Figure 4b**). In contrast, the ^{13}C direct excitation scheme is viable at RT but suffers from long ^{13}C relaxation times (>10 s) and low sensitivity, necessitating acquisition times on the order of 20-30 hours.[137] While directly excited RT ^{13}C spectra can resolve the perovskite (e.g. $MAPbI_3$ and $FAPbI_3$) and unreacted precursors (MAI, FAI, respectively), RT ^{13}C chemical shifts are insensitive to phase composition (e.g. the MA/FA ratio).[137] These advantageous features of ^{1}H-^{13}C CP cryo-NMR have allowed us to provide atomic-level proof of guanidinium incorporation into MA- and FA-based MHPs, putting to rest a long-standing debate over whether or not it incorporates into the structure (**Figure 4b-c**).[20] The ease of detection and short experiment times make cryo-NMR a perfectly suited tool for routine investigation of new multi-cation MHPs materials. For example, we have applied it to evidence the formation of layered FA 2D/3D MHPs with adamantyl-based spacers and found (a) the formation of new FA environments

corresponding to FA directly interacting with the spacer, and (b) that increasing the FA/spacer ratio leads to progressively more locally disordered spacer environments, rather than a locally well-defined structure (**Figure 5a**).[49,167] The formation of new FA environments interacting with the spacer is corroborated by the ^{1}H-^{15}N CP data (**Figure 5b**) and together with the diffraction data allowed for a structural model of the layered phase to be established (**Figure 5c**). ^{15}N is a 0.4% abundant spin I=1/2 nucleus with receptivity just 2% of that of ^{13}C, which makes its detection challenging even in bulk MHP samples at RT. However, the sensitivity benefits of cryo-NMR make the detection of ^{1}H-^{15}N CP spectra from MHPs viable.

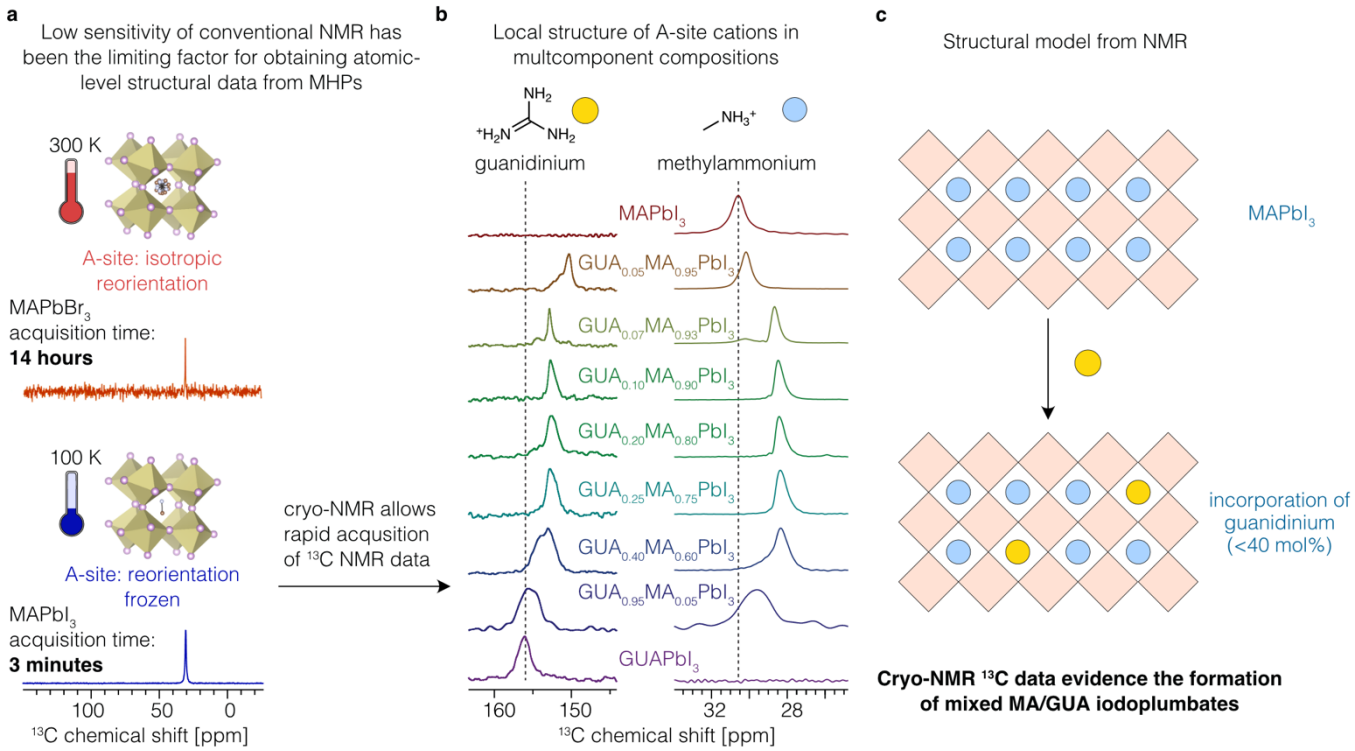

Figure 4. Phase composition in hybrid MHPs from ^{13}C and ^{15}N cryo-NMR. (a) RT vs 100 K ^{13}C MAS NMR spectra demonstrating the substantial sensitivity improvement brought about by carrying out the measurement at cryogenic temperatures, (b) ^{1}H-^{13}C CP cryo-NMR data of GUA/MA MHPs showing the evolution of the GUA and MA local environment as a function of their ratio.[20] The shift of the MA signal on introducing GUA into the composition is atomic-level proof of their mixing in the structure. (c) Structural model of GUA/MA mixing. The ^{13}C spectrum of $MAPbBr_3$ in panel (a) was adapted with permission.[42] 2016, Royal Chemical Society. Adapted with permission.[20] 2018, 2019, American Chemical Society..

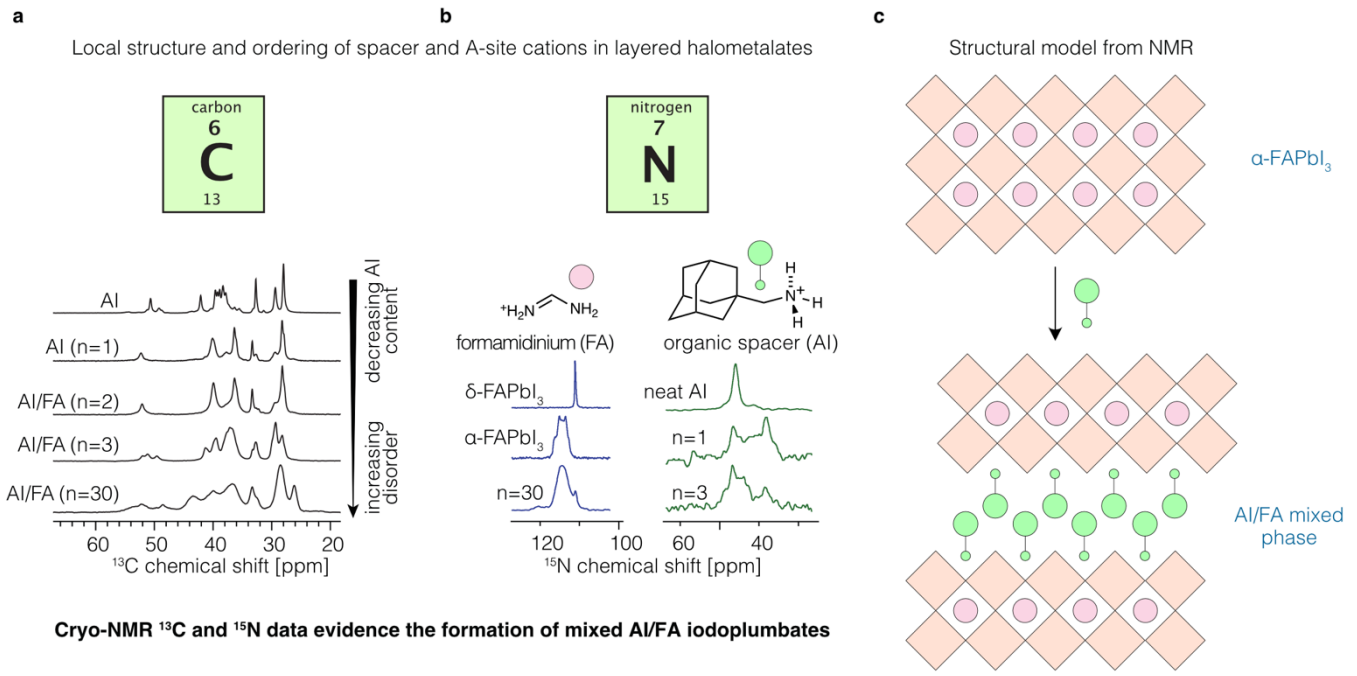

Figure 5. Phase composition in layered iodoplumbates from ^{13}C and ^{15}N cryo-NMR. (a) 100 K ^{1}H-^{13}C CP cryo-NMR data of layered 2D/3D FA-based perovskites using an adamantyl-based spacer.[49] The data evidence the increasing disorder as the FA/AI ratio increases visible as progressive broadening of the resonances. (b) The corresponding ^{1}H-^{15}N CP cryo-NMR spectra which corroborate the increasing disorder. Adapted with permission.[49] 2019, Wiley. (c) Structural model of the mixed AI/FA iodoplumbate.

5.4 Phase composition of caesium-containing hybrid and all-inorganic perovskites: ^{133}Cs MAS NMR

Caesium in compositions with FA and MA has emerged as an essential component of MHPs for optoelectronics applications,[168] while all-inorganic caesium MHPs, $CsPbX_3$ (X=I, Br), have been used as a more thermally stable alternative.[21] The atomic-level microstructure of these materials can be conveniently probed using solid-state ^{133}Cs MAS NMR. ^{133}Cs is a 100% abundant spin I=7/2 nucleus with receptivity 284 times higher than that of ^{13}C and a very small quadrupole moment, which makes it straightforward to obtain high SNR spectra from diluted samples and thin films. Since quantification requires data acquisition with a recycle delay of at least $5 \cdot T_1$, it is essential to verify the T_1 of all Cs-containing phases present within the sample of interest and set this parameter based on the slowest relaxing species, which may have a T_1 in excess of 100 s. ^{133}Cs shifts span a wide range of ~500 ppm, which translates to superior spectral resolution of different structures (**Figure 6a**).

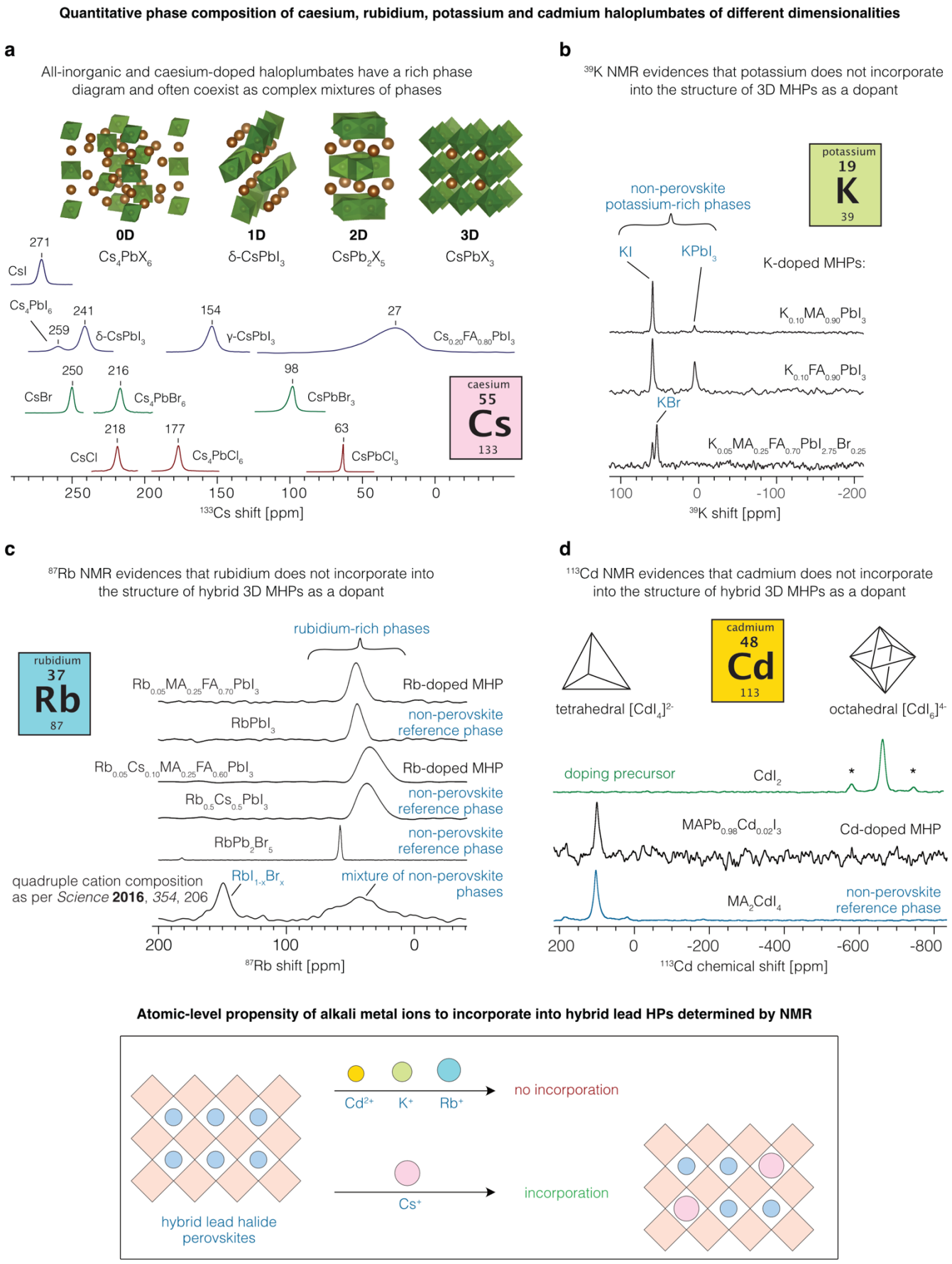

Figure 6. **Speciation of diamagnetic metal ion dopants in MHPs.** (a) ^{133}Cs MAS NMR data for caesium-containing halides and haloplumbates exemplifying the remarkable spectral resolution achievable in this

technique that allows quantification of caesium-containing phases in multi-phase mixtures. Note that the ^{133}Cs spectra shown here have a relative shift of -13 ppm with respect to those reported by Karmakar et al. due to a difference in referencing (here, δ=0 ppm for 1M aqueous solution of CsCl).[50] (b-c) ^{39}K and ^{87}Rb MAS NMR data for rubidium and potassium doped MHPs, respectively. The only Rb- and K-containing phases in doped 3D MHPs are segregated non-perovskite phases – there is no incorporation of rubidium and potassium into the 3D perovskite structure of MHPs. (d) ^{113}Cd MAS NMR distinguishes between tetrahedral and octahedral coordination environments. There is no incorporation of Cd^{2+} into hybrid MHPs. Adapted with permission.[19,26,134] 2017, 2018, 2020, American Chemical Society.

5.4.1 Cs-doped hybrid perovskites

Incorporation of Cs^+ into hybrid MHPs has been previously evidenced using XRD where it leads to compelling shifts on the order of ~0.07° per every 10 mol% Cs^+ replacing FA^+ in the crystal structure.[169] We have evaluated Cs/FA mixing using ^{133}Cs MAS NMR and found that Cs^+ inside the $FAPbI_3$ lattice yields a characteristic peak between 10-40 ppm with its large width consistent with static disorder, *i.e.* the presence of a distribution of different combinations of Cs^+ and FA^+ in the neighbouring cubooctahedral cages (**Figure 6a**, $Cs_{0.20}FA_{0.80}PbI_3$).[19] This broad spectral signature is also present in more complex multicomponent materials such as Cs/MA/FA iodide-bromide and chloride-doped MHPs.[138] Incorporation of Cs^+ can be corroborated in a ^{1}H-^{133}Cs heteronuclear correlation (HETCOR) experiment relying on dipolar coupling between the Cs^+ and FA cations.[19]

5.4.2 All-inorganic $CsPbX_3$ (X=I, Br, Cl) perovskites

The CsX-PbX_2 (X=I, Br, Cl) phase diagram contains multiple phases whose structure is determined by the type of halide (**Figure 6a**). The presence of multiple halides leads to static disorder and considerably broader peaks, as has been shown for $CsPbBr_{1.5}Cl_{1.5}$[138] and $CsPbI_2Br$[21]. A library of ^{133}Cs MAS NMR spectra of single- and mixed-halide ternary caesium haloplumbates has been reported, including all the known non-perovskite phases, complemented by ^{207}Pb NMR data.[50]

^{133}Cs MAS NMR has provided insight into the lively debated origin of green fluorescence in Cs_4PbBr_6.[170–172] Several reports have shown that bulk and nanocrystalline Cs_4PbBr_6 exhibits strong green fluorescence and identified it as intrinsic to the parent 0D lattice while others ascribed it to impurities such as the 3D perovskite $CsPbBr_3$ which also exhibits green fluorescence. ^{133}Cs MAS NMR has been used to characterize Cs_4PbBr_6 NCs synthesized using different conditions and reported a phase-pure 0D material with no detectable 3D perovskite phase.[170] These authors ascribed the green fluorescence to the presence of speculated 2D Cs_2PbBr_4 monolayer inclusions which were however not detected experimentally. The debate on the origin of green fluorescence in Cs_4PbBr_6 is therefore still wide open. Indeed, in other solid-state NMR studies, it has been consistently observed that the only bromoplumbate phases formed within the $CsBr$-$PbBr_2$ ternary phase diagram for various precursor ratios are $CsPbBr_3$, Cs_4PbBr_6, an impurity phase (likely $CsPb_2Br_5$) or their mixtures, consistent with the data available in the ICSD database. Surface-selective ^{133}Cs NMR has been used to determine the surface termination of $CsPbBr_3$ nanocubes.[173] It has also been applied to study phosphonate-capped $CsPbBr_3$ nanoplatelets and provided a unique picture of the complexity of their surface with distinct features seemingly corresponding to different facets and/or ligand binding modes.[174] While the approach of elucidation of the atomic-level structure of nanocrystal surfaces from their solid-state NMR spectra, and linking the structure to their properties has been extensively employed in classic inorganic semiconductor nanocrystals[85,175] this has only very recently started to be developed for hybrid and all-inorganic MHPs.

6 Phase segregation of additives which do not incorporate into MHPs

Following the success of caesium doping in improving stability and optoelectronic properties, other alkali and alkaline earth metals have been explored as additives: rubidium,[176] potassium,[177] sodium,[178] lithium,[179] barium,[180,181] strontium,[180,182–185] calcium[180,186] and magnesium[185,187,188]. Unlike for caesium doping, in these cases the XRD powder patterns were, to within experimental error, identical for doped and undoped $MAPbI_3$ while relative shifts of XRD reflections were observed only when doping mixed-halide compositions. We hypothesized that this may be owing to phase segregation of the additive, which leads to changes in the iodide-to-bromide ratio in the perovskite lattice. This may arise because the lattice parameter of mixed-HPs is a strong function of the I-to-Br ratio. For example, in a measurement employing a Cu K-α X-ray source, the main perovskite peak shifts from about 2θ=14° in $MAPbI_3$ to about 15° in $MAPbBr_3$ and takes on intermediate values in mixed-halide $MAPbI_{3-x}Br_x$ compositions, roughly 0.1° per every +10 mol% change in the halide ratio.[189] This effect is even more pronounced for higher order reflections. We have investigated speciation of the two most widely used additives, rubidium and potassium, using ^{87}Rb and ^{39}K MAS NMR, respectively, and found that neither of these two cations incorporates into the structure of lead MHPs.[19,26] In another study, we also looked at speciation of barium in $CsPbI_2Br$ and demonstrated that while it does not incorporate, it manifestly leads to changes in the intended I:Br ratio, which is the direct reason for the experimentally observed variation in optoelectronics properties.[27] We view the effect of K^+ and Rb^+ addition as largely based on the same principle, whereby these cations may bind excess halides leading to a form of halide sequestration, which affects the defect density of the main MHP phase. In the same vein, we have recently elucidated that BF_4^- does not incorporate into $MAPbI_3$ but rather it acts as a scavenger of excess MAI with which it forms a separate stable cocrystal phase.[146] Since Rb^+ and K^+ are additives which do not incorporate into the 3D MHP structure, we highlight that the stoichiometries of the corresponding solid materials should always be referred to as *formal* stoichiometries. More generally, solid-state NMR speciation studies should be carried out whenever a new additive or a new composition are introduced.

6.1 Rubidium speciation: ^{87}Rb MAS NMR

^{87}Rb is a 28% abundant spin I=3/2 nucleus with receptivity 290 times higher than that of ^{13}C and a moderate quadrupole moment, allowing high sensitivity detection even in mass-limited samples. Rubidium iodoplumbate, $RbPbI_3$, is the only rubidium-containing phase detected in compositions formally denoted as $Rb_{0.05}FA_{0.95}PbI_3$, $Rb_{0.10}FA_{0.90}PbI_3$. and $Rb_{0.05}MA_{0.25}FA_{0.70}PbI_3$ (**Figure 6c**).[19] A more complex situation results in the presence of caesium, for example in materials formally denoted as $Rb_{0.05}Cs_{0.10}FA_{0.80}PbI_3$ and $Rb_{0.05}Cs_{0.10}MA_{0.25}FA_{0.65}PbI_3$. In these cases, the formation of a mixed-cation $Rb_{1-x}Cs_xPbI_3$ non-perovskite phase competes with the incorporation of caesium into the 3D perovskite lattice.[19] The resulting structural and optoelectronic changes are therefore caused by the depletion of caesium from rather than incorporation of rubidium into the 3D perovskite lattice. Finally, when mixed-halide (I/Br) compositions are doped with rubidium, there exist more possible non-perovskite phases: $RbPbI_3$, $RbPb_2Br_5$ and another previously undescribed bromide phase along with their mixed-halide analogues. We have identified a mixture of all these possible non-perovskite phases along with unreacted RbI and RbBr in the quadruple-cation composition reported previously.[176] The ^{87}Rb MAS NMR results have thereby unambiguously shown that there is no rubidium incorporation into the 3D perovskite lattice of organic-inorganic MHPs, settling the debate on its speciation in these materials. The result indicating a lack of rubidium incorporation has been corroborated using EDX SEM elemental mapping.[190]

6.2 Potassium speciation: ^{39}K MAS NMR

^{39}K is a 39% abundant spin I=3/2 nucleus with receptivity 3 times higher than that of ^{13}C and a moderate quadrupole moment. The use of the highest available magnetic fields is therefore essential to provide

practical sensitivity. The added benefit of using high magnetic fields for studying half-integer quadrupolar nuclei is that the linewidth of their central transition is inversely proportional to the strength of the magnetic field, yielding a significant extra boost in both resolution and sensitivity. While bulk samples of KI, $KPbI_3$ and related materials from the KBr-$PbBr_2$ phase diagram can be detected within minutes, sensitive detection in dilute potassium-doped perovskites may take up to 20-40 hours. We have applied ^{39}K MAS NMR to study speciation of potassium in potassium-doped $MAPbI_3$, $MA_{1-x}FA_xPbI_3$, caesium-containing and mixed-halide compositions as well as all-inorganic $CsPbI_2Br$ (**Figure 6b**).[26] We have found that while there is no incorporation of potassium into any of these materials, the non-perovskite products that form strongly depend on the exact composition of the main perovskite phase. In potassium-doped MA/FA iodoplumbates ($MA_{1-x}FA_xPbI_3$), the only potassium-containing species were unreacted KI and $KPbI_3$. Doping a mixed-halide iodide/bromide MA/FA material with KI led to a mixture of KI and KBr, indicating that KI preferentially reacts with bromides, extracting them from the parent 3D perovskite lattice. This result rationalizes the previously observed potassium-induced shifts in optical spectra and X-ray diffraction peaks of mixed-halide materials as being due to changes in the iodide-to-bromide ratio in the 3D MHP phase and is qualitatively identical to that observed for rubidium doping. The presence of caesium leads to the formation of mixed-cation $K_{1-x}Cs_xPbI_3$ non-perovskite phases which change the initial perovskite composition by depleting it of caesium. The same effect is observed in all-inorganic $CsPbI_2Br$ whereby a complex mixture of non-perovskite $K_{1-x}Cs_xPbI_{3-y}Br_y$ is formed. In each of these cases it is possible to support the speciation of caesium by ^{133}Cs MAS NMR which quantitatively shows the amount of caesium in the perovskite and non-perovskite phases. These results have been subsequently corroborated using HAADAF STEM elemental mapping.[177] ^{133}Cs and ^{39}K MAS NMR measurements have been used to elucidate speciation of potassium in K-doped $CsPbBr_3$/Cs_4PbBr_6 light-emitting materials.[191] While the 3D and 0D phases form concurrently, their molar ratio in the undoped and potassium-doped composition are considerably different. The authors found that potassium is only incorporated into the lattice of the 0D phase, Cs_4PbBr_6, to yield $Cs_{4-x}K_xPbBr_6$ which acts as a matrix for nanocrystals of the 3D phase, $CsPbBr_3$.

Finally, we note that while ^{87}Rb and ^{39}K MAS NMR provide information on speciation of the respective elements in the solid perovskite material, their speciation in DMF/DMSO-based precursor solutions is a separate subject. The atomic-level mechanism of action of these additives might be related to their effect on processes such as nucleation and subsequent crystallite growth through their effect on the molar ionic strength of the precursor solution as well as ion-ion-solvent interactions of the dissolved haloplumbate aggregates.[192,193] Liquid-state NMR ^{87}Rb and ^{39}K studies are expected to provide more insight into processes occurring at these stages of growth.

6.3 Cadmium speciation: ^{113}Cd MAS NMR

The addition of cadmium ions has been proposed as a method of band gap tuning and suppressing vacancies responsible for degradation in MHPs.[194–197] Using the same principles as for the other elements discussed above, we have very recently applied ^{113}Cd MAS NMR at 21.1 T to investigate speciation of cadmium in various MHPs.[134] We have found that Cd^{2+} is not incorporated into $MAPbI_3$ and FA-based mixed-cation (Cs, MA, FA) lead mixed-halide (I, Br) perovskites down to 1 mol% doping level but rather forms non-perovskite halocadmate phases, MA_2CdI_4 or $(MA/FA)_2Cd(I,Br)_4$, in contrast to previous conclusions on cadmium incorporation based on XPS.[197] On the other hand, we have found that Cd^{2+} incorporates into $CsPbBr_3$ via Cd^{2+}-for-Pb^{2+} substitution up to around 10 mol%, consistent with the previous HAADF STEM results.

7 B-site doping and halide coordination environments

In this section, we summarise the recent progress on B-site doping by paramagnetic ions and the use of ^{207}Pb NMR to indirectly study the ordering of halides.

7.1 Transition metal doping

Incorporation of Mn^{2+} and Eu^{2+} into $CsPbX_3$ (X=Cl, Br, I)

Transition metals and lanthanides are widely employed to enhance luminescence and stability of $CsPbCl_3$, $CsPbBr_3$ and mixed-halide perovskite nanocrystals.[198–202] We have used Eu^{2+} doping to improve performance and stability of $CsPbI_2Br$ solar cells,[21] and developed a simple solid-state NMR strategy allowing routine investigation of paramagnetic doping into MHPs. If a paramagnetic dopant is incorporated into the perovskite lattice, it causes substantial shortening of the ^{133}Cs longitudinal relaxation time T_1. Paramagnetic relaxation enhancement (PREs) is caused by dipole-dipole interactions between the nuclear spins (e.g. of ^{133}Cs) and the unpaired electron spins of the dopant (e.g. Mn^{2+}, Eu^{2+}) and are therefore an atomic-level probe of incorporation of the dopant into the perovskite lattice (**Figure 7a**).[203] This effect can be explored by measuring the longitudinal build-up curve (**Figure 7b-c**). While the build-up is yields a monoexponential T_1 for undoped materials, it becomes stretched for perovskites doped with paramagnetic species (here Mn^{2+}) owing to the presence of a distribution of relaxation times within the material, varying as a function of the ^{133}Cs-Mn^{2+} distance. The build-up curves are measured using increments equally spaced on the logarithmic scale so as to evidence the possible presence of fast- and slow-relaxing components. In this way, we have demonstrated using ^{133}Cs relaxation the incorporation of Mn^{2+} into the perovskite structures of $CsPbBr_3$ (**Figure 7b**) and $CsPbCl_3$, as well as Eu^{2+} into $CsPbI_2Br$. Further, the distribution of the dopants can be determined by modelling different incorporation scenarios, and in the cases studied we found no dopant clustering, consistent with the previously reported HAADF-STEM maps.[202] Complementary information on the local structure of Mn^{2+} in the Mn-doped perovskite can be obtained from Electron Spin Resonance (ESR), which directly probes the transition metal ion.[139]

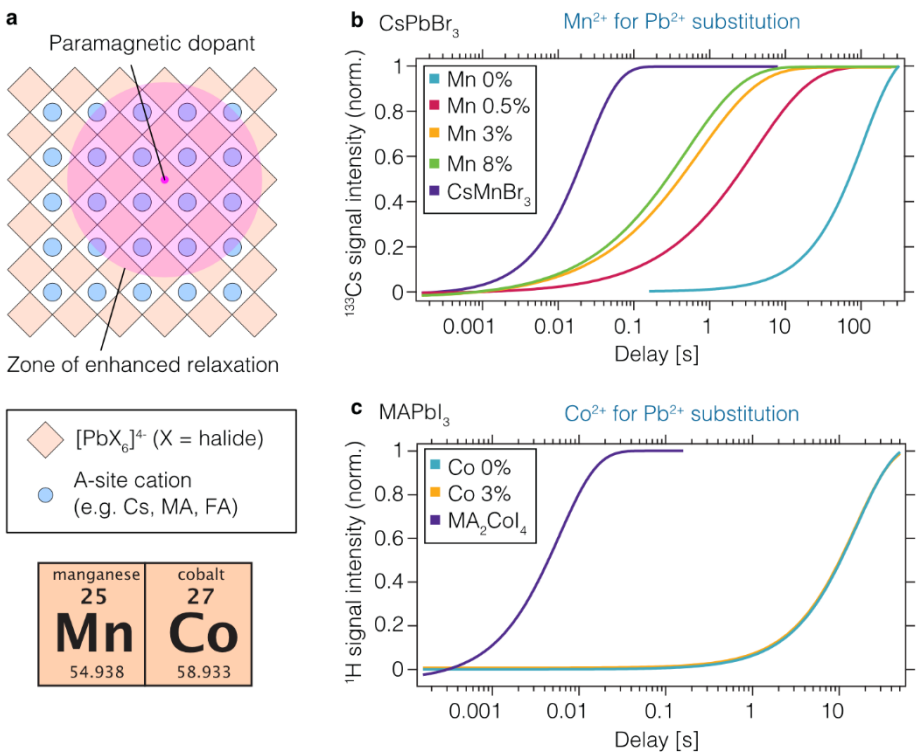

Figure 7. Speciation of paramagnetic metal ion dopants in MHPs. (a) A schematic representation of the paramagnetic relaxation enhancement (PRE). T_1 build-up curve for (b) ^{133}Cs in $CsPbBr_3$, (c) ^{1}H in $MAPbI_3$

in which Pb^{2+} was gradually replaced by Mn^{2+}, and Co^{2+} respectively. The presence of Mn^{2+} in the perovskite structure leads to a pronounced PRE visible as faster return of the magnetisation to equilibrium. There is no PRE in the case of Co-doped $MAPbI_3$. While Mn^{2+} incorporates into the perovskite structure of $CsPbBr_3$, there is no incorporation of Co^{2+} into $MAPbI_3$. Adapted with permission.[139] 2019, Royal Chemical Society.

No incorporation of Co^{2+} into $MAPbI_3$

The PRE strategy is not limited to ^{133}Cs as a probe. In principle any NMR active nucleus will experience a PRE from a nearby paramagnetic dopant. Co^{2+} has been identified as a promising solar cell modulator and suggested it incorporates into the perovskite lattice of $MAPbI_3$ as a B-site dopant.[204] We have subsequently investigated Co^{2+} speciation in this composition.[139] Here, the ^{1}H T_1 build-up curve evidenced that the build-up time of the perovskite phase is essentially unchanged (**Figure 7c**), while a strong relaxation enhancement is expected for Co^{2+} incorporated in a close proximity of the MA protons in the lattice.[203] This result has unambiguously shown that there is no Co^{2+} incorporation into the structure of $MAPbI_3$ and an alternative explanation has to be sought to rationalize the optoelectronic improvements and structural changes observed. It is worth noting that the study by Klug et al. used acetate metal precursors to perform metal ion doping. However, the interaction of the acetate ion with MHPs and thus its possible contribution to the observed changes has not yet been elucidated at the atomic level and is therefore an open question.

Incorporation of Cu^{2+} into $Cs_2SbAgCl_6$.

Beyond PREs, the incorporation of paramagnetic dopants may lead to paramagnetic shifts.[203] A new lead-free double-perovskite material has been recently developed in which Cu^{2+} doping leads to a considerable lowering of the band gap with respect to the pristine $Cs_2SbAgCl_6$ (~1 and 2.6 eV, respectively).[25] The authors used ^{133}Cs MAS NMR to investigate the atomic-level structure of the pristine and Cu^{2+}-doped materials and found that incorporation of Cu^{2+} leads to the appearance of new caesium environments corresponding to sites with one and two Cu^{2+} nearest neighbours. The magnitude of the paramagnetic shift is directly related to the atomic-level mechanism of interaction between the caesium site and the Cu^{2+} dopant and provides evidence that there is a degree of covalency in the Cs^{+} interaction with the $[SbAgCl_6]^{2-}$ sublattice mediated by p- and d-type orbitals (Fermi contact shift).[203]

7.2 Halide coordination environments: ^{207}Pb MAS NMR

Halogens in MHPs are characterised by high asymmetry of the local electronic environment leading to high quadrupolar coupling constants (C_Q) and in turn very broad NMR spectra. Direct acquisition of halogen NMR spectra is therefore challenging and has only recently been demonstrated.[150] The large C_Q's make halide NQR a more preferable approach although its wider applicability to new materials is somewhat impeded by the comparable difficulty of finding the resonance frequency for an arbitrary halide coordination environment.[44,150] The halide composition can be probed more readily in an indirect manner using lead NMR since the Pb^{2+} sites in MHPs are involved in the formation of covalent octahedral lead halide environments. ^{207}Pb is a 22% abundant spin I=1/2 nucleus with receptivity 12 times higher than that of ^{13}C, which allows facile detection in bulk perovskite samples. A library of ^{207}Pb MAS NMR spectra of single- and mixed-halide $MAPbX_3$ perovskites (X=I, Br, Cl) has been reported which shows that ^{207}Pb chemical shifts and line widths are highly sensitive to the halide coordination environment of the lead site and therefore can be used to probe phase segregation and halide speciation in materials prepared using different processing protocols (**Figure 8a**).[28,42] They also observed that the ^{207}Pb longitudinal relaxation time, T_1, is similar for all single-halide perovskites (~1 s) for a static sample, but that a substantial decrease

of T_1 occurs for $MAPbI_3$ (0.08 s) and $MAPbBr_3$ (0.1 s) under MAS. This result was rationalized in terms of the MAS-induced halogen polarization exchange T_1 relaxation mechanism[205] and is an important experimental consideration as it allows for the use of significantly shorter recovery delays, which shortens the necessary experiment time (**Figure 2a**).

This analysis has been extended to a series of mixed-halide $MAPbCl_{3-x}Br_x$ materials in which the Cl/Br ratio was varied in small steps.[30] ^{207}Pb NMR spectra on this group of compounds evidenced the formation of distinct $[PbBr_6]^{4-}$, $[PbBr_5Cl]^{4-}$, $[PbBr_4Cl_2]^{4-}$, $[PbBr_3Cl_3]^{4-}$, $[PbBr_2Cl_4]^{4-}$, $[PbBrCl_5]^{4-}$ and $[PbCl_6]^{4-}$ coordination environments, each of which was resolved in the ^{207}Pb spectrum (**Figure 8b**). The authors used 2D ^{207}Pb-^{207}Pb SD measurements to evidence that all the coordination environments originate from a single solid solution phase. Analogous analysis was carried out for $MAPbI_{3-x}Br_x$, although in this case the signals are considerably broader, which is ascribed to the presence of a ^{207}Pb-^{127}I J-coupling and renders the resolution of different $[PbI_{6-x}Br_x]^{4-}$ environments impossible. Single- and mixed-halide $FAPbX_3$ (X=I, Br, Cl) materials have been subsequently investigated and exhibited analogous behaviour.[29] Also in this case the authors used 2D ^{207}Pb-^{207}Pb SD to evidence the formation of a solid solution of halides rather than a phase-segregated physical mixture (**Figure 8c**).

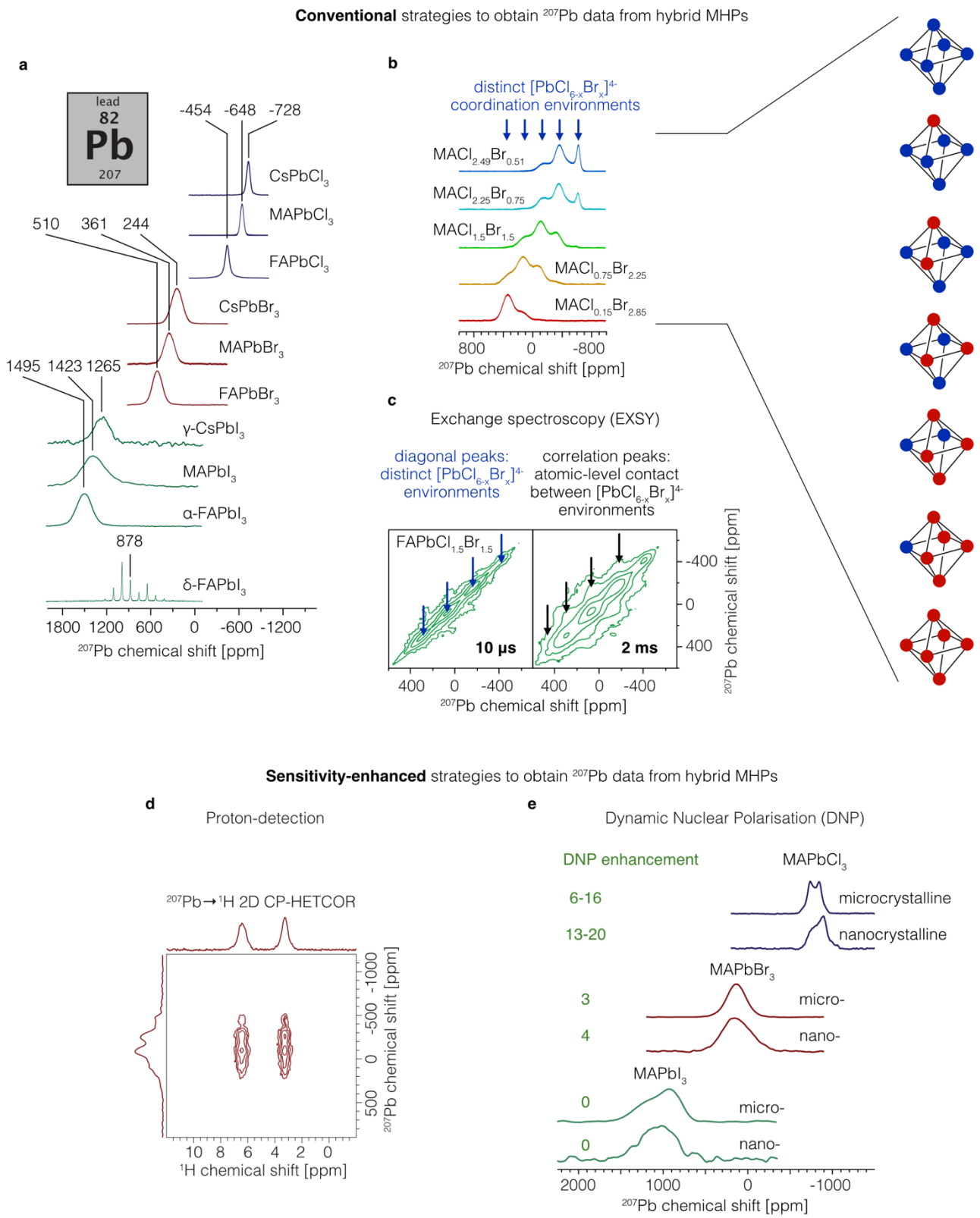

Figure 8. ^{207}Pb solid-state NMR lead HPs as a means of probing lead-halide coordination and halide mixing. (a) 1D spectra of 3D single-halide lead HPs demonstrating that the ^{207}Pb chemical shift is highly sensitivity to the type of halide and, to a smaller degree, to the type of A-site cation. (b) 1D spectra of mixed-halide $MAPbCl_{3-x}Br_x$ materials showing resolved local lead environments corresponding to different Cl/Br ratios within an octahedron, (c) a 2D ^{207}Pb-^{207}Pb SD spectrum of $FAPbCl_{1.5}Br_{1.5}$ evidencing fast magnetization exchange between different local $[PbX_6]^{4-}$ coordination environments and thereby supporting the formation of a solid solution in which the different local environments are in atomic-level

contact (the mixing times are indicated in bold; longer mixing times lead to correlation signals from more distant environments, on the order of <50Å). Sensitivity-enhanced NMR strategies allow detection from mass-limited samples (e.g. thin films). (d) A ^{207}Pb-^{1}H 2D CP-HETCOR spectrum of $MAPbCl_{1.5}Br_{1.5}$ as an example of a sensitive way of detecting ^{207}Pb spectra from MHPs. In proton-detected approaches, the ^{207}Pb signals is detected *via* the more sensitive ^{1}H nuclei. (e) DNP is a general way of enhancing sensitivity in solid-state NMR by a factor of up to about 660. However, its application to MHPs has been faced with problems. DNP-enhanced ^{207}Pb spectra of micro- and nanocrystalline MHPs demonstrating the challenge associated with hyperpolarization in this class of materials. Adapted with permission.[29,30,37,50,57] 2017-2020, American Chemical Society

An important question related to ^{207}Pb NMR is whether or not it can be reliably used to indirectly study the A-site cation composition. A summary of ^{207}Pb chemical shifts reported for $CsPbX_3$, $MAPbX_3$ and $FAPbX_3$ (X=I, Br, Cl) offers an insight into this point (**Figure 8a**).[28–30] It is clear that ^{207}Pb can be used to distinguish between Cs, MA and FA chlorides and bromides. The difference between iodides is considerably smaller (<230 ppm) and given the large line width (~300 ppm) as well as strong temperature dependence of the shift, we conclude that it is not possible to reliably resolve Cs, MA and FA lead iodides using ^{207}Pb NMR. The strong temperature dependence of the ^{207}Pb chemical shift in $MAPbCl_3$ has also been used as an advantage to accurately measure temperature in MAS NMR experiments.[206]

^{207}Pb MAS NMR can be used to distinguish between α-$FAPbI_3$ and δ-$FAPbI_3$ and the resolution is sufficient to resolve these two phases in a mixture.[37] Interestingly, while MAS does not significantly affect the ^{207}Pb line shape of the 3D perovskite phases $MAPbI_3$ and α-$FAPbI_3$ (fwhm ~22-26 kHz), it leads to the appearance of a well-resolved chemical shift anisotropy (CSA) pattern in δ-$FAPbI_3$ (fwhm ~1 kHz, **Figure 8a**) made using mechanosynthesis suggesting that either (a) ^{207}Pb-^{127}I J-coupling is not the reason behind the broadening observed in $MAPbI_3$ and α-$FAPbI_3$ or (b) this interaction is self-decoupled in δ-$FAPbI_3$. In this context, it is also important to invoke another recent result. A ^{207}Pb spectrum of a solution-processed δ-$FAPbI_3$ recorded under MAS has been reported in which the CSA pattern is not resolved suggesting that the synthesis protocol may slightly affect the local structure.[207] We also note that the two measurements were carried out at different temperatures. Finally, ^{207}Pb MAS NMR has also been used to analyse the degradation products of $MAPbI_3$ and allowed the identification the $MAPbI_3$ mono- and dihydrate which allowed kinetic studies of the degradation process.[36]

While obtaining ^{207}Pb spectra on bulk perovskite powders is straightforward, mass-limited samples pose a challenge. An in-depth study of sensitivity-enhancing protocols relying on fast-spinning MAS and Dynamic Nuclear Polarization (DNP)[92] has been performed using $MAPbBr_3$ as a model compound.[57] The authors identified proton-detected ^{207}Pb→^{1}H CP-HETCOR experiments as currently the best way of increasing sensitivity at room temperature (a factor of 41 higher sensitivity compared to directly detected ^{207}Pb spin echo) and demonstrated this strategy to enhance sensitivity in a mixed-halide material, $MAPbBr_{1.5}Cl_{1.5}$ (**Figure 8d**). Low-temperature approaches, including DNP, also provide considerable enhancements. That said, while DNP has been used to enhance NMR sensitivity of materials by factors of over 200,[95,208,209] it does not perform nearly as well in the case of MHPs, yielding enhancements of 10-20 for $MAPbCl_3$, 3-4 for $MAPbBr_3$ and no enhancement at all for $MAPbI_3$ due to very short (<1 s) ^{1}H T_1's under typical MAS DNP conditions (i.e. at 100 K), which prevents efficient relayed DNP (**Figure 8e**). The successful application of MAS DNP to MHPs with enhancements on the order of 100-200 remains one of the open challenges in the field as it would allow highly sensitive NMR detection of perovskite dopants present well below 1 mol% in thin film compositions.

8 Local structure and redox chemistry of tin(II) MHPs: ^{119}Sn MAS NMR

^{119}Sn (spin I = ½) is the most receptive of the three NMR-active isotopes of tin with a receptivity about 27 times that of ^{13}C. Some of the most fundamental and unusual properties of tin(II) MHPs, such as dynamic local cation off-centring, are the result of the stereochemical activity of the Sn^{2+} lone pair,[210,211] and can be tuned by compositional changes.[212] However, until very recently, there were no studies of the local structure in this class of materials using ^{119}Sn NMR. Static variable-temperature ^{119}Sn NMR has been first applied to study halide self-diffusion in $MASnBr_3$ and $FASnI_3$.[213] We extended this approach by employing ^{119}Sn MAS to characterize the local structure and redox chemistry of mixed-cation and mixed-halide tin MHPs, products of their degradation, as well as various related non-perovskite phases.[31] The key challenge was to realise that the longitudinal relaxation of ^{119}Sn strongly depends on the halide compositions and spans 6 orders of magnitude in this class of compounds, which makes careful choice of experimental parameters essential to record spectra. We have shown that ^{119}Sn readily distinguishes between the +2 and +4 oxidation state in these systems with the corresponding chemical shift difference being nearly 5500 ppm between $MASnI_3$ and MA_2SnI_6, and 1700 ppm between $MASnBr_3$ and MA_2SnBr_6, and that it is sensitive to the halide ratio in mixed-halide compositions. In addition, we used variable-temperature ^{119}Sn T_1 relaxation measurements at multiple magnetic fields to establish the activation energy for bromide hopping in $MASnBr_3$. Interestingly, we have found that the tin(IV) site in MA_2SnI_6 is exceptionally deshielded, with an unprecedented chemical shift of -4684 ppm, while iodide-containing materials exhibit remarkably broad lines, spanning about 2500 ppm for the pure tin(II) iodide perovskites which we tentatively ascribed to coupling to the highly quadrupolar ^{127}I nucleus. However, very recently, a highly resolved ^{119}Sn spectrum of microcrystalline $MASnI_3$ prepared in solution in the presence of the strongly reducing hypophosphorous acid, H_3PO_2 has been reported (**Figure 9a**).[214] The spectral signature of this material has been found to evolve over time after exposure to air yielding unknown intermediate products whose NMR spectrum matches well that of $MASnI_3$ prepared using mechanosynthesis in the absence of reducing agents in our study. Therefore, while the long-range structure of $MASnI_3$ prepared in the presence and absence of H_2PO_3, as probed by XRD, is the same, the local ^{119}Sn environment strongly depends on the synthesis conditions. Potential factors contributing to this include spontaneous disproportionation of the material prepared in the absence of reducing agents leading to disorder and the emergence of metallicity.[215] Very recently, ^{119}Sn has been evidence the formation of a solid solution with fully random Sn/Pb arrangements in $CsSn_xPb_{1-x}Br_3$ for any Sn/Pb ratio.[216]

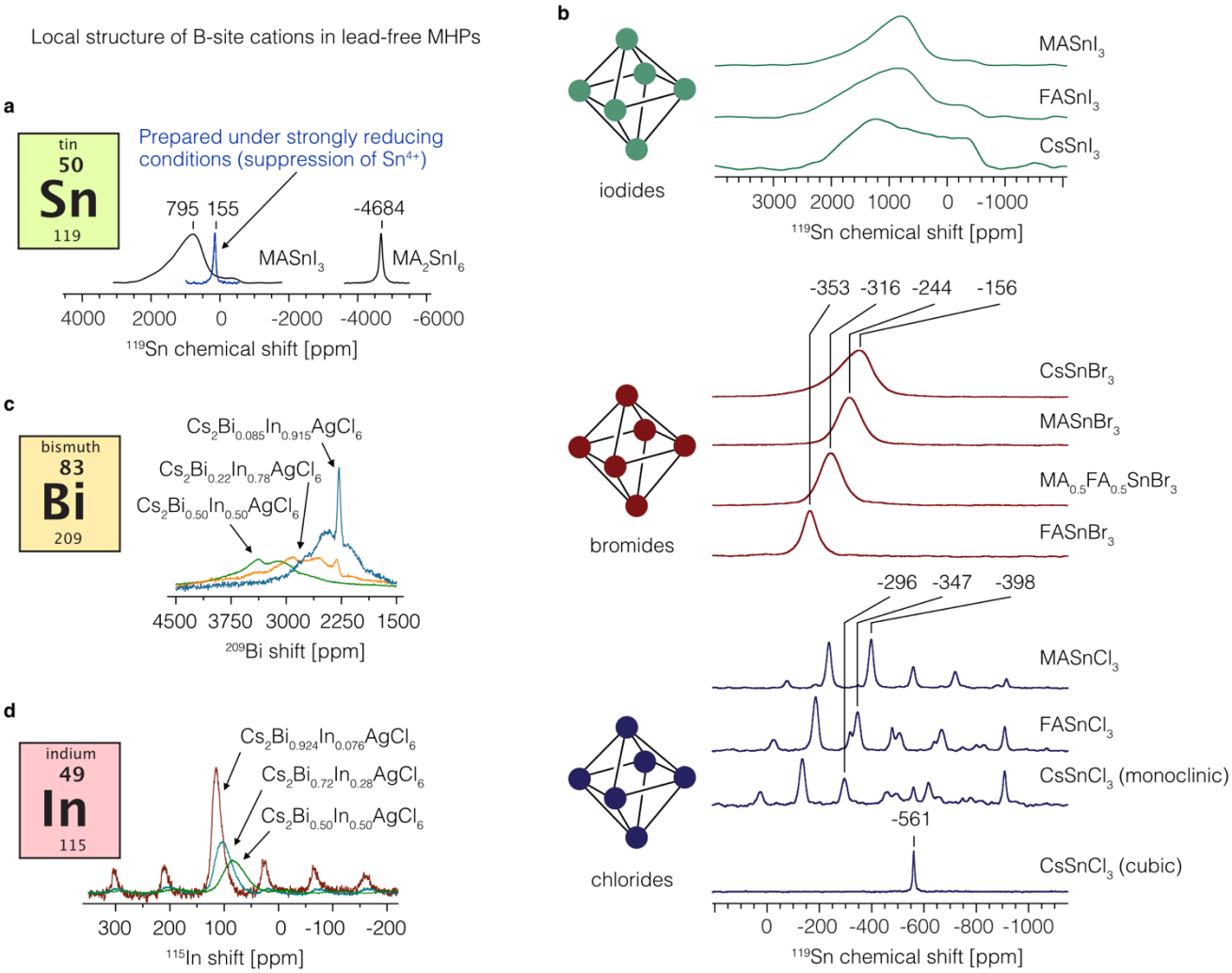

Figure 9. Solid-state NMR of B-site cations in MHPs. (a) ^{119}Sn spectra of $MASnI_3$ prepared in the presence and absence of a strong reducing agent (H_3PO_2), and of MA_2SnI_6, as an example of the sensitivity of ^{119}Sn NMR to the tin oxidation state, (b) ^{119}Sn spectra of tin(II) halide perovskites with various A-site cations and halides illustrating the sensitivity of the ^{119}Sn chemical shift and line shape to the local environment (c) ^{209}Bi and (d) ^{115}In spectra from $Cs_2Bi_{1-x}In_xAgCl_6$ double MHPs recorded at 21 T evidencing Bi/In mixing and illustrating the challenge associated with substantial EFG broadening when these nuclei are present in asymmetric local environments. Adapted with permission.[24,31] 2020, American Chemical Society

9 Local structure and B-site mixing in silver-indium-bismuth double perovskites: ^{115}In, ^{209}Bi

Indium (^{115}In, 96%, spin I = 9/2) and bismuth (^{209}Bi, 100% abundant, spin I = 9/2) are highly sensitive NMR-active nuclei. A comprehensive solid-state NMR study of bismuth-indium mixing in $Cs_2Bi_{1-x}In_xAgCl_6$ double perovskites has recently been reported.[24] The study has shown that the simple endmembers, $Cs_2BiAgCl_6$ and $Cs_2InAgCl_6$, show no evidence of Ag/Bi and Ag/In anti-site disorder since ^{115}In and ^{209}Bi in these materials show vanishingly small quadrupole coupling constants (C_Q). C_Q is a sensitive probe of local symmetry whereby any departure from ideal octahedral coordination and local ordering would lead to dramatic line broadening for these two nuclei. The fact that the C_Q is not strictly zero can be ascribed to the presence of a low concentration of halide vacancies which are stable point defects in halide double perovskites. Further, the authors combined solid-state ^{209}Bi/^{115}In NMR with DFT

quadrupolar parameter calculations and X-ray diffraction to unambiguously show that the In^{3+}/Bi^{3+} distribution in $Cs_2Bi_{1-x}In_xAgCl_6$ is fully random (*i.e.* there is no preferential clustering of either In^{3+} or Bi^{3+}) for all Bi:In ratios (**Figure 9c,d**). The study was complemented by ^{133}Cs data. We have very recently investigated halide mixing in closely related Cs_2AgBiX_6 (X = Cl, Br, and I) materials using ^{133}Cs NMR and established their full binary halide mixing phase diagram.[217]

10 The effect of dopants on the symmetry of the A-site cation cages: ^{14}N MAS NMR

^{14}N is a 99.6% abundant spin I=1 nucleus with receptivity 100 times higher than that of ^{13}C and a moderate quadrupole moment. However, as a spin I=1, it does not possess a central transition making it necessary to acquire the whole quadrupolar pattern which may span up to 7.5 MHz for highly asymmetric ^{14}N environments.[218,219] Well-established ultra-wide line acquisition protocols makes the task feasible.[220]

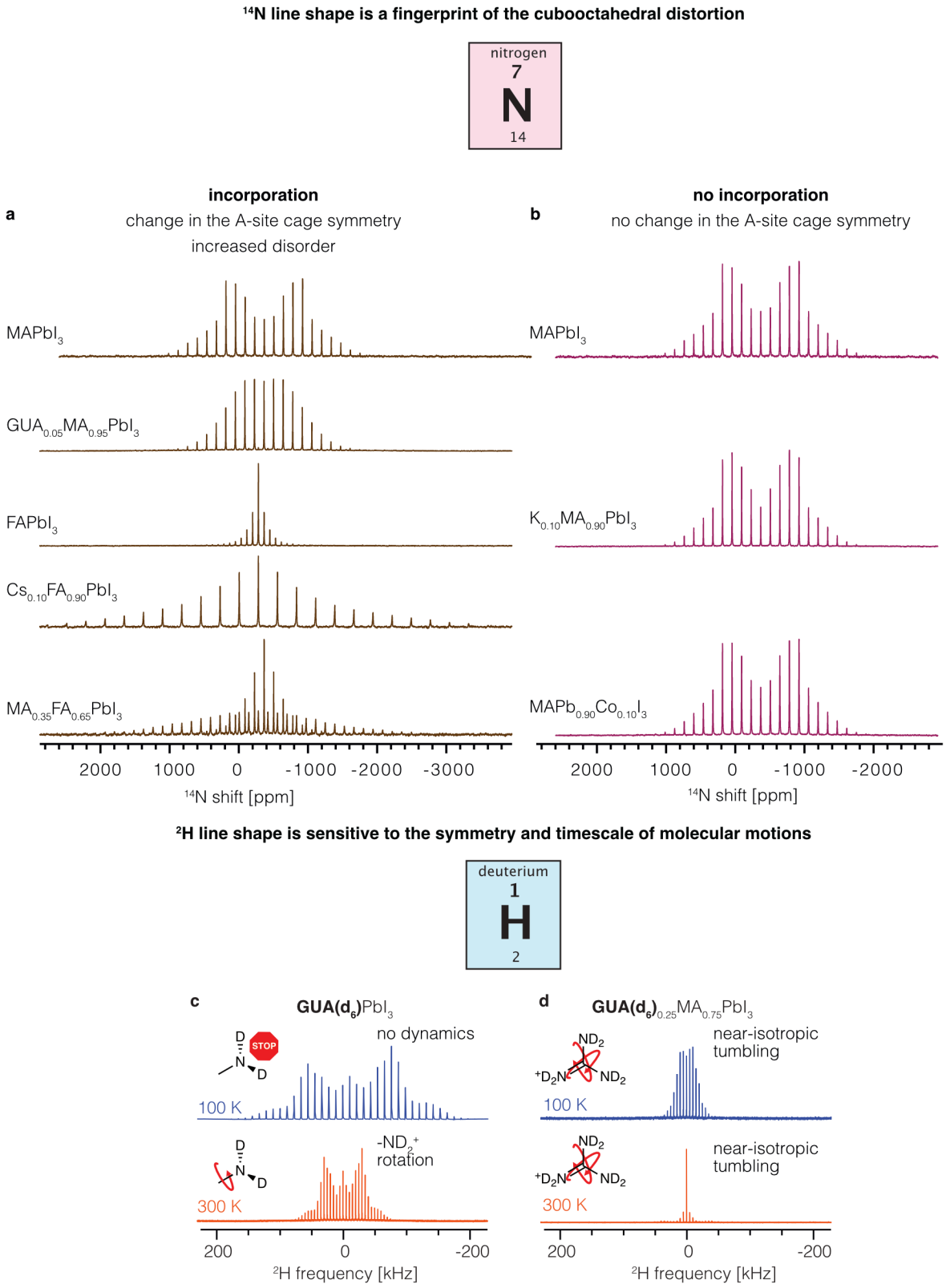

Figure 10. **Incorporation of dopants and motional degrees of freedom as probed by nuclei sensitive to dynamics.** (a) The shape of the ^{14}N MAS NMR spectrum is highly sensitive to the local symmetry of the cavity in which the A-site cation (e.g. MA or FA) is reorienting. Any change made to the structure of the material, for example by incorporating dopants, has a substantial effect on the spectrum as it changes the local symmetry. This effect is demonstrated here by comparing pristine $MAPbI_3$ and $FAPbI_3$ to the corresponding materials doped with small amounts of guanidinium (GUA), caesium and to a mixed MA/FA material. (b) Conversely, addition of ions which do not incorporate into the perovskite structure

does not affect the local symmetry, as illustrated here for the case of potassium and cobalt added to $MAPbI_3$. This result serves to corroborate the lack of capacity of these dopants to incorporate into the structure of $MAPbI_3$. | Variable-temperature ^2H NMR measurements are the most common approach to study dynamics in solids as the ^2H line shapes strongly depend on the correlation time and symmetry of motion. These effects are illustrated here by (c) $GUA(d_6)PbI_3$ (a 1D non-perovskite phase) which is fully rigid at 100 K while acquires a degree of freedom at room temperature ($-ND_2^+$ rotation), and (d) $GUA(d_6)_{0.25}MA_{0.75}PbI_3$ (a mixed-cation 3D perovskite phase), which exhibits near-isotropic tumbling of GUA across the 100-300 K temperature range. The exact time scale and symmetry can be obtained from the spectra by simulations, as described in the original work. Adapted with permission.[19,20,22,37] 2017-2019, American Chemical Society.

However, the width of a ^{14}N spectrum can be considerably smaller than expected based on the structural asymmetry. This arises if there are dynamic processes present which reorient the electric field gradient (EFG) tensor of the ^{14}N nucleus at a rate which is comparable to or faster than the inverse of the quadrupolar coupling constant, C_Q, e.g. 200 ns for a C_Q=5 MHz. This is the case in liquids as well as some ionic solids such as NaCN[221] and MHPs,[6] where the CN^- anion and organic A-site cation, respectively, are reorienting on the picosecond timescale in a cubic or nearly cubic local environment. In these cases, the shape of the ^{14}N spectrum is not determined by the static C_Q value, which would have been the case in the absence of motion, but rather by the asymmetry of the local environment, which in NaCN and KCN is due to lattice defects[221,222] while in MHPs is a highly sensitive probe of the deviation from the native symmetry of the A-site cage of the undoped materials.[37] We have demonstrated this by acquiring ^{14}N MAS NMR spectra of $MAPbI_3$ below and above the tetragonal-to-cubic phase transition. We have observed an analogous effect on cooling in $FAPbI_3$,[37] consistent with the $\alpha \rightarrow \beta$ phase transition which lowers the crystallographic symmetry.[223]

Consequently, ^{14}N can be used to indirectly probe cation incorporation into MHPs. A-site cation mixing leads to a pronounced decrease in local symmetry which is reflected in the broadening of the spinning sideband (SSB) manifolds in the mixed-cation samples (**Figure 10a**). We have demonstrated that the local symmetry decreases upon incorporation of Cs^+ into $FAPbI_3$,[19] GUA into $MAPbI_3$ and $FAPbI_3$,[20] MA into $FAPbI_3$,[37] and when 2D/3D layered perovskite phases are formed[49,167]. The lowering of the A-site cation cage symmetry in $FA_{1-x}Cs_xPbI_3$ has been recently predicted by *ab initio* molecular dynamics simulations and is in agreement with the experimental ^{14}N data.[224] Changes in the symmetry have also been observed in 3D MHPs doped with small amounts of organic molecular modulators,[34,167] even if the molecules are not incorporated into the 3D perovskite structure but rather reside on its surface.[34] Conversely, no appreciable change in the shape of the ^{14}N SSB manifold has been observed for dopants which do not incorporate into the 3D perovskite structure, such as K^+ and Co^{2+} (**Figure 10b**).

11 Cation Dynamics: ^2H and ^{14}N MAS NMR

^2H (deuterium) is a 0.01% abundant spin I = 1 nucleus with a receptivity of only 1% that of ^{13}C and a moderate quadrupole moment. The low natural abundance requires isotopic enrichment which is straightforward for exchangeable protons. ^2H is the most widely used probe of dynamics in solid state NMR spectroscopy since its line shape and relaxation are very sensitive to dynamics occurring in the millisecond to nanosecond regime.[116,225,226] ^2H NMR of $MAPbX_3$ (X=I, Br, Cl) was first used to study phase transitions and A-site cation ordering in single-halide MHPs.[6] This model has been recently refined and apparent activation energies for the dynamics in the three single-halide perovskite materials in cubic and tetragonal phases were reported.[39] We have reported ^2H MAS data for $FA(d_4)_{0.67}MA(d_3)_{0.33}PbI_3$ and found that rotation

of the ND_3 and ND_2 fragments around the C–N bond is very fast (correlation time $\tau_c < 10^{-6}$ s) down to 100 K.[37] We have also applied this framework to study the degrees of freedom of GUA in $GUAPbI_3$ (a 1D non-perovskite phase) and when it is incorporated into the 3D perovskite lattice of $MAPbI_3$, in $GUA_{0.25}MA_{0.75}PbI_3$ (**Figure 10c-d**),[20] as well to evaluate the dynamics of large organic adamantyl-based spacers in layered 2D/3D perovskite materials.[49] While the neat spacer, AI-d_3, showed a classic spin $I = 1$ pattern expected for an ammonium salt and indicative of only -ND_3^+ rotation, additional degrees of freedom were present in the layered FA-based iodoplumbate structure which led to considerable decrease in the effective ^{2}H EFG anisotropy, which we identified be due to wobbling of the adamantyl backbone. Very recently, ^{2}H NMR has been employed to evidence the formation of metastable $MAPbI_{3-x}Cl_x$ solid solutions, thereby settling the long-standing debate on chloride incorporation into $MAPbI_3$.[227]

Beyond the structural information discussed above, ^{14}N can also be used to study dynamics and since its quadrupole coupling constants are significantly larger than those of ^{2}H, the lineshape is sensitive to faster motions, in the ns to ps regime.[116] The local dynamic behaviour of the A-site cation is of considerable fundamental interest as it contributes to the dielectric properties of the material.[228] In a seminal work, the correlation times of MA in $MAPbX_3$ (X=I, Br, Cl) have been reported.[6] We have applied ^{14}N MAS NMR to mixed A-site cation MA/FA compositions to show that the correlation time of the two cations within the same material can be probed independently using the same motional model owing to the spectral resolution provided by MAS.[37] To that end, we have used the model-free approach developed by Lipari and Szabo in which the motion is described by only two adjustable parameters.[229,230] We have found significant differences in the correlation time of MA and FA within this model. These results were subsequently debated based on ^{1}H relaxation of $FAPbI_3$,[41] meta-analysis of ^{1}H relaxation data of $MAPbI_3$,[41] and ^{14}N relaxation data of $MAPbI_3$,[39] pointing out that there are no significant changes in the correlation time of MA and FA in these two perovskite phases, using a different approach to the motional model. Further studies are required to refine the models for dynamics in these deceptively complex systems. Similarly, we have applied the model-free approach to calculate the correlation time of GUA in a mixed-cation GUA/MA 3D perovskite. The theoretical framework developed by Lipari and Szabo is applicable to other, more complex MHPs and could, for example, corroborate the prediction that incorporation of caesium leads to a significant reduction in the FA tumbling frequency.[224] Very recently, ^{1}H and ^{14}N NMR has been applied to elucidate the changes in dynamics of FA in $Cs_xFA_{1-x}PbBr_3$ as a function of the caesium content and proposed that caesium doping removes cooperative changes in dynamic degrees of freedom of FA which in turn leads to suppression of clear-cut phases transitions.[141]

12 Outlook

Fundamental understanding of the atomic-level mechanism of action of organic and inorganic additives is currently the limiting factor in the development of perovskite-based solar cell and LEDs. In order to rationally design new materials on-demand, it is essential to fully understand the structure-activity relationships in the existing and newly developed MHP compositions. Solid-state NMR has clearly established itself as the technique of choice for studying microstructure and structural dynamics in hybrid and all-inorganic halide perovskites, in particular owing to its capacity to quantitatively detect highly disordered and amorphous phases, including surface species. A broad range of experimental protocols have now been developed which make its routine application to a broad range of systems straightforward. There still remain areas where it can be further developed to provide a comprehensive description of previously reported but poorly understood phenomena. This in particular concerns the application of $^{6/7}$Li, ^{23}Na, ^{43}Ca, ^{87}Sr, ^{137}Ba and ^{25}Mg NMR to reveal speciation of the respective metal ion dopants in MHPs. Mechanistic understanding of Cl^- incorporation into iodide-based lead MHPs, and compelling evidence for its presence or absence after thermal annealing,[231] are yet to be demonstrated at the atomic level, potentially using $^{35/37}$Cl

NMR and NQR. We expect that faster and more accurate DFT calculations of NMR parameters will play a key role in aiding dopant speciation studies. Paramagnetic NMR protocols have opened up new opportunities for studying incorporation of essentially any transition metal or lanthanide into the structure of MHPs. While a number of sensitivity-enhancing protocols have been developed for rapid detection of ^{207}Pb spectra, the most promising technique, MAS DNP, remains untapped as it has so far been surprisingly inefficient in this class of materials. Further developments in this area, leading to enhancements on the order of 100-200, comparable to those seen in other microcrystalline organic and inorganic solids, are expected to be a game changer for MAS NMR characterization of defects, surface passivation agents and dilute dopants in MHPs. Beyond sensitivity, the resolution of ^{207}Pb spectra of iodide-containing MHPs is subpar with respect to that of compositions based on other halides, the reasons behind which are not sufficiently well understood. Since the MHP compositions most pertinent to solar cell research are iodide-rich, it is essential to fully elucidate the cause of the ^{207}Pb line broadening and put forward methods to reduce it. ^{119}Sn NMR is expected to allow detailed mechanistic studies of redox-active agents which are essential for obtaining efficient tin-based optoelectronic devices, which will be critical components of all-perovskite tandem solar cells, for example. The effect the synthetic route has on self-doping in tin halide perovskites and how it changes over time are yet to be elucidated. This insight has the potential to drive the development of more stable tin-based materials. In the same vein, exploring the impact of different synthetic routes on the local structure may help understand the subtle differences in materials properties obtained using solution-, solid-state and vapour deposition. The local structure and dynamics of cations in new intrinsically disordered classes of hybrid halide materials, such as hollow perovskites, will be an important area of solid-state NMR research. There is a great potential for NMR crystallography methods either employing quantitative spin-diffusion dynamics or using chemical shift driven approaches in combination with DFT shift calculations to provide structural constraints in cases which are difficult to access using diffraction methods. A key example is the thin organic layers used as passivation agents for MHPs. Mechanisms of photodegradation, in particular when coupled with exposure to air, are still poorly understood at the atomic level. In particular, the development of high-resolution NMR strategies to study operating devices, albeit technically challenging, will be a game changer for the understanding of degradation mechanisms. In addition, we expect solid-state NMR to have a great impact on the understanding of other solar cell and LED components such as the hole and electron transport layers (HTL and ETL, respectively). These interfaces are critical for the device performance and stability and their presence may change the surface properties of the absorber material altogether. Since charge transport is critically dependent on the quality of the perovskite/HTL and perovskite/ETL interface, studies of these interfaces using MAS DNP are expected to provide insights into their atomic-level structure of similar importance to those previously reported for interfaces and surface sites in catalysts, nanocrystals and interfaces in hybrid bioinorganic materials, yielding for the first time structure-activity relationships at the atomic level in these challenging-to-characterise materials. Finally, we believe that it is essential to correlate local structural information from multiple complementary techniques – solid-state NMR, NQR, μSR, X-ray and neutron total scattering, X-ray absorption spectroscopy (XAS) and ESR – to develop a truly comprehensive and self-consistent atomic-level picture of new materials. We expect that further technical and material developments will continue to drive rich atomic-level insight into these important semiconductor materials, helping to drive them towards new unforeseen applications and commercialization.

Acknowledgements

This work has received funding from the European Union's Horizon 2020 research and innovation programme under the Marie Skłodowska-Curie grant agreement No. 841136. This work was supported by

Swiss National Science Foundation Grant No. 200020_178860. S.D.S. acknowledges the Royal Society and Tata Group (UF150033). CPG acknowledges the Royal Society.

Author contributions

D.J.K. wrote the article with contributions from S.D.S., C.P.G., and L.E.

Competing interests

The authors declare no competing interests.

References

1. Weber, D. CH3NH3PBX3, A Pb(II)-system with cubic perovskite structure. *Z. Naturforschung Sect. B- J. Chem. Sci.* **33**, 1443–1445 (1978).
2. Wasylishen, R. E., Knop, O. & Macdonald, J. B. Cation rotation in methylammonium lead halides. *Solid State Commun.* **56**, 581–582 (1985).
3. Poglitsch, A. & Weber, D. Dynamic Disorder In Methylammoniumtrihalogenoplumbates(Ii) Observed By Millimeter-wave Spectroscopy. *J. Chem. Phys.* **87**, 6373–6378 (1987).
4. Onodayamamuro, N., Matsuo, T. & Suga, H. Calorimetric and IR spectroscopic studies of phase-transitions in methylammonium trihalogenoplumbates-(Ii). *J. Phys. Chem. Solids* **51**, 1383–1395 (1990).
5. Furukawa, Y. & Nakamura, D. Cationic dynamics in the crystalline phases of (CH3NH3)PbX3 (x=Cl, Br). *Z. Naturforschung Sect. - J. Phys. Sci.* **44**, 1122–1126 (1989).
6. Knop, O., Wasylishen, R. E., White, M. A., Cameron, T. S. & Van Oort, M. J. M. Alkylammonium lead halides. Part 2. CH3NH3PbX3 (X = chlorine, bromine, iodine) perovskites: cuboctahedral halide cages with isotropic cation reorientation. *Can. J. Chem.* **68**, 412–22 (1990).
7. Xu, Q., Eguchi, T., Nakayama, H., Nakamura, N. & Kishita, M. Molecular motions and phase-transitions in solid CH3NH3PbCl3, CH3NH3PbBr3, CH3NH3PbI3, as studied by NMR and NQR. *Z. Naturforschung Sect. - J. Phys. Sci.* **46**, 240–246 (1991).
8. Xu, Q., Eguchi, T. & Nakayama, H. Molecular motions in solid CD3NH3PbBr3 as studied by H-1-NMR. *Bull. Chem. Soc. Jpn.* **65**, 2264–2266 (1992).
9. Mitzi, D. B., Feild, C. A., Harrison, W. T. A. & Guloy, A. M. Conducting tin halides with a layered organic-based perovskite structure. *Nature* **369**, 467–469 (1994).

10. Auger, V. & Karantassis, T. Sels complexes de l'iodure stanneux avec les iodures de rubidium et de caesium. *Compt Rend* **181**, 665–666 (1925).

11. Møller, C. The structure of caesium plumbo iodide CsPbI3. *Mat Fys Medd Dan Vid Selsk* **32**, (1959).

12. Kojima, A., Teshima, K., Shirai, Y. & Miyasaka, Tsutomu. Organometal Halide Perovskites as Visible-Light Sensitizers for Photovoltaic Cells. *J. Am. Chem. Soc.* **131**, 6050–6051 (2009).

13. Etgar, L. *et al.* Mesoscopic CH 3NH 3PbI 3/TiO 2 heterojunction solar cells. *J. Am. Chem. Soc.* **134**, 17396–17399 (2012).

14. Lee, M. M., Teuscher, J., Miyasaka, T., Murakami, T. N. & Snaith, H. J. *Science* **338**, 643–647 (2012).

15. https://www.nrel.gov/pv/cell-efficiency.html. https://www.nrel.gov/pv/.

16. Lin, K. *et al.* Perovskite light-emitting diodes with external quantum efficiency exceeding 20 per cent. *Nature* **562**, 245–248 (2018).

17. Ma, D. *et al.* Chloride Insertion–Immobilization Enables Bright, Narrowband, and Stable Blue-Emitting Perovskite Diodes. *J. Am. Chem. Soc.* **142**, 5126–5134 (2020).

18. Chen, B., N. Rudd, P., Yang, S., Yuan, Y. & Huang, J. Imperfections and their passivation in halide perovskite solar cells. *Chem. Soc. Rev.* **48**, 3842–3867 (2019).

19. Kubicki, D. J. *et al.* Phase Segregation in Cs-, Rb- and K-Doped Mixed-Cation (MA)x(FA)1–xPbI3 Hybrid Perovskites from Solid-State NMR. *J. Am. Chem. Soc.* **139**, 14173–14180 (2017).

20. Kubicki, D. J. *et al.* Formation of Stable Mixed Guanidinium–Methylammonium Phases with Exceptionally Long Carrier Lifetimes for High-Efficiency Lead Iodide-Based Perovskite Photovoltaics. *J. Am. Chem. Soc.* **140**, 3345–3351 (2018).

21. Xiang, W. *et al.* Europium-Doped CsPbI 2 Br for Stable and Highly Efficient Inorganic Perovskite Solar Cells. *Joule* **3**, 205–214 (2019).

933 22. Kubicki, D. J. *et al.* Doping and phase segregation in Mn2+- and Co2+-doped lead halide
934 perovskites from 133Cs and 1H NMR relaxation enhancement. *J. Mater. Chem. A* **7**, 2326–2333
935 (2019).
936 23. Franssen, W. M. J., Bruijnaers, B. J., Portengen, V. H. L. & Kentgens, A. P. M. Dimethylammonium
937 Incorporation in Lead Acetate Based MAPbI3 Perovskite Solar Cells. *ChemPhysChem* **19**, 3107–
938 3115 (2018).
939 24. Karmakar, A., Bernard, G. M., Meldrum, A., Oliynyk, A. O. & Michaelis, V. K. Tailorable Indirect
940 to Direct Band-Gap Double Perovskites with Bright White-Light Emission: Decoding Chemical
941 Structure Using Solid-State NMR. *J. Am. Chem. Soc.* (2020) doi:10.1021/jacs.0c02198.
942 25. Karmakar, A., Dodd, M. S., Agnihotri, S., Ravera, E. & Michaelis, V. K. Cu(II)-Doped
943 Cs2SbAgCl6 Double Perovskite: A Lead-Free, Low-Bandgap Material. *Chem. Mater.* **30**, 8280–
944 8290 (2018).
945 26. Kubicki, D. J. *et al.* Phase Segregation in Potassium-Doped Lead Halide Perovskites from 39K
946 Solid-State NMR at 21.1 T. *J. Am. Chem. Soc.* **140**, 7232–7238 (2018).
947 27. Xiang, W. *et al.* Ba-induced phase segregation and band gap reduction in mixed-halide inorganic
948 perovskite solar cells. *Nat. Commun.* **10**, 1–8 (2019).
949 28. Rosales, B. A. *et al.* Persistent Dopants and Phase Segregation in Organolead Mixed-Halide
950 Perovskites. *Chem. Mater.* **28**, 6848–6859 (2016).
951 29. Askar, A. M. *et al.* Composition-Tunable Formamidinium Lead Mixed Halide Perovskites via
952 Solvent-Free Mechanochemical Synthesis: Decoding the Pb Environments Using Solid-State NMR
953 Spectroscopy. *J. Phys. Chem. Lett.* **9**, 2671–2677 (2018).
954 30. Karmakar, A. *et al.* Mechanochemical Synthesis of Methylammonium Lead Mixed–Halide
955 Perovskites: Unraveling the Solid-Solution Behavior using Solid-State NMR. *Chem. Mater.* **30**,
956 2309–2321 (2018).

31. Kubicki, D. J. *et al.* Local Structure and Dynamics in Methylammonium, Formamidinium, and Cesium Tin(II) Mixed-Halide Perovskites from 119Sn Solid-State NMR. *J. Am. Chem. Soc.* **142**, 7813–7826 (2020).

32. Alharbi, E. A. *et al.* Atomic-level passivation mechanism of ammonium salts enabling highly efficient perovskite solar cells. *Nat. Commun.* **10**, 1–9 (2019).

33. Alanazi, A. Q. *et al.* Atomic-Level Microstructure of Efficient Formamidinium-Based Perovskite Solar Cells Stabilized by 5-Ammonium Valeric Acid Iodide Revealed by Multinuclear and Two-Dimensional Solid-State NMR. *J. Am. Chem. Soc.* **141**, 17659–17669 (2019).

34. Bi, D. *et al.* Multifunctional molecular modulators for perovskite solar cells with over 20% efficiency and high operational stability. *Nat. Commun.* **9**, 4482 (2018).

35. Hong, L. *et al.* Guanine-Stabilized Formamidinium Lead Iodide Perovskites. *Angew. Chem. Int. Ed.* (2019).

36. Askar, A. M., Bernard, G. M., Wiltshire, B., Shankar, K. & Michaelis, V. K. Multinuclear Magnetic Resonance Tracking of Hydro, Thermal, and Hydrothermal Decomposition of CH3NH3PbI3. *J. Phys. Chem. C* **121**, 1013–1024 (2017).

37. Kubicki, D. J. *et al.* Cation Dynamics in Mixed-Cation (MA)x(FA)1-xPbI3 Hybrid Perovskites from Solid-State NMR. *J. Am. Chem. Soc.* **139**, 10055–10061 (2017).

38. Franssen, W. M. J., van Es, S. G. D., Dervisoglu, R., de Wijs, G. A. & Kentgens, A. P. M. Symmetry, Dynamics, and Defects in Methylammonium Lead Halide Perovskites. *J. Phys. Chem. Lett.* **8**, 61–66 (2017).

39. Bernard, G. M. *et al.* Methylammonium Cation Dynamics in Methylammonium Lead Halide Perovskites: A Solid-State NMR Perspective. *J. Phys. Chem. A* **122**, 1560–1573 (2018).

40. Senocrate, A. *et al.* The Nature of Ion Conduction in Methylammonium Lead Iodide: A Multimethod Approach. *Angew. Chem. Int. Ed.* **56**, 7755–7759 (2017).

41. Fabini, D. H. *et al.* Universal Dynamics of Molecular Reorientation in Hybrid Lead Iodide Perovskites. *J. Am. Chem. Soc.* **139**, 16875–16884 (2017).

42. Roiland, C. *et al.* Multinuclear NMR as a tool for studying local order and dynamics in CH3NH3PbX3 (X = Cl, Br, I) hybrid perovskites. *Phys. Chem. Chem. Phys.* **18**, 27133–27142 (2016).

43. Franssen, W. M. J. & Kentgens, A. P. M. Solid–state NMR of hybrid halide perovskites. *Solid State Nucl. Magn. Reson.* **100**, 36–44 (2019).

44. Piveteau, L., Morad, V. & Kovalenko, M. V. Solid-state NMR and NQR Spectroscopy of Lead-Halide Perovskite Materials. *J. Am. Chem. Soc.* (2020) doi:10.1021/jacs.0c07338.

45. Prochowicz, D. *et al.* Mechanosynthesis of the hybrid perovskite CH3NH3PbI3: Characterization and the corresponding solar cell efficiency. *J. Mater. Chem. A* **3**, 20772–20777 (2015).

46. Prochowicz, D. *et al.* Mechanosynthesis of pure phase mixed-cation MA: XFA1- xPbI3 hybrid perovskites: Photovoltaic performance and electrochemical properties. *Sustain. Energy Fuels* **1**, 689–693 (2017).

47. Rosales, B. A., Wei, L. & Vela, J. Synthesis and mixing of complex halide perovskites by solvent-free solid-state methods. *J. Solid State Chem.* **271**, 206–215 (2019).

48. Prochowicz, D., Saski, M., Yadav, P., Grätzel, M. & Lewiński, J. Mechanoperovskites for Photovoltaic Applications: Preparation, Characterization, and Device Fabrication. *Acc. Chem. Res.* **52**, 3233–3243 (2019).

49. Milić, J. V. *et al.* Supramolecular Engineering for Formamidinium-Based Layered 2D Perovskite Solar Cells: Structural Complexity and Dynamics Revealed by Solid-State NMR Spectroscopy. *Adv. Energy Mater.* **0**, 1900284 (2019).

50. Karmakar, A. *et al.* Mechanochemical synthesis of 0D and 3D cesium lead mixed halide perovskites. *Chem. Commun.* **55**, 5079–5082 (2019).

51. Saski, M., Prochowicz, D., Marynowski, W. & Lewiński, J. Mechanosynthesis, Optical, and Morphological Properties of MA, FA, Cs-SnX3 (X = I, Br) and Phase-Pure Mixed-Halide MASnIxBr3–x Perovskites. *Eur. J. Inorg. Chem.* **2019**, 2680–2684 (2019).

1008 52. Palazon, F. *et al.* Mechanochemical synthesis of inorganic halide perovskites: evolution of phase-
1009 purity, morphology, and photoluminescence. *J. Mater. Chem. C Mater. Opt. Electron. Devices* **7**,
1010 11406–11410 (2019).
1011 53. Zhu, Z.-Y. *et al.* Solvent-Free Mechanosynthesis of Composition-Tunable Cesium Lead Halide
1012 Perovskite Quantum Dots. *J. Phys. Chem. Lett.* **8**, 1610–1614 (2017).
1013 54. Protesescu, L., Yakunin, S., Nazarenko, O., Dirin, D. N. & Kovalenko, M. V. Low-Cost Synthesis
1014 of Highly Luminescent Colloidal Lead Halide Perovskite Nanocrystals by Wet Ball Milling. *ACS*
1015 *Appl. Nano Mater.* **1**, 1300–1308 (2018).
1016 55. Stoumpos, C. C., Malliakas, C. D. & Kanatzidis, M. G. Semiconducting tin and lead iodide
1017 perovskites with organic cations: Phase transitions, high mobilities, and near-infrared
1018 photoluminescent properties. *Inorg. Chem.* **52**, 9019–9038 (2013).
1019 56. Li, T., Dunlap-Shohl, W. A., Han, Q. & Mitzi, D. B. Melt Processing of Hybrid Organic–Inorganic
1020 Lead Iodide Layered Perovskites. *Chem. Mater.* **29**, 6200–6204 (2017).
1021 57. Hanrahan, M. P., Men, L., Rosales, B. A., Vela, J. & Rossini, A. J. Sensitivity-Enhanced 207Pb
1022 Solid-State NMR Spectroscopy for the Rapid, Non-Destructive Characterization of Organolead
1023 Halide Perovskites. *Chem. Mater.* **30**, 7005–7015 (2018).
1024 58. Bloch, F. Nuclear induction. *Phys. Rev.* **70**, 460–474 (1946).
1025 59. Purcell, E., Torrey, H. & Pound, R. Resonance absorption by nuclear magnetic moments in a solid.
1026 *Phys. Rev.* **69**, 37–38 (1946).
1027 60. Reif, B., Ashbrook, S. E., Emsley, L. & Hong, M. Solid-state NMR. *Nat. Rev. Methods Primer* (in
1028 press).
1029 61. Gil, A. M. & Neto, C. P. Solid-State Nmr Studies Of Wood And Other Lignocellulosic Materials. in
1030 *Annual Reports on NMR Spectroscopy* (ed. Webb, G. A.) vol. 37 75–117 (Academic Press, 1999).
1031 62. Terrett, O. M. *et al.* Molecular architecture of softwood revealed by solid-state NMR. *Nat. Commun.*
1032 **10**, 4978 (2019).

63. Blümich, B., Hagemeyer, A., Schaefer, D., Schmidt-Rohr, K. & Spiess, H. W. Solid State NMR spectroscopy in polymer science. *Adv. Mater.* **2**, 72–81 (1990).

64. MacKenzie, K. J. D. & Smith, M. E. *Multinuclear Solid-State Nuclear Magnetic Resonance of Inorganic Materials*. (Elsevier, 2002).

65. Ashbrook, S. E., Griffin, J. M. & Johnston, K. E. Recent Advances in Solid-State Nuclear Magnetic Resonance Spectroscopy. *Annu. Rev. Anal. Chem.* **11**, 485–508 (2018).

66. Moran, R. F. *et al.* Ensemble-Based Modeling of the NMR Spectra of Solid Solutions: Cation Disorder in Y2(Sn,Ti)2O7. *J. Am. Chem. Soc.* **141**, 17838–17846 (2019).

67. Youngman, R. NMR Spectroscopy in Glass Science: A Review of the Elements. *Materials* **11**, 476 (2018).

68. Tricot, G., Alpysbay, L. & Doumert, B. Solid State NMR: A Powerful Tool for the Characterization of Borophosphate Glasses. *Molecules* **25**, 428 (2020).

69. Jiang, J. *et al.* Synthesis and Structure Determination of the Hierarchical Meso-Microporous Zeolite ITQ-43. *Science* **333**, 1131–1134 (2011).

70. Peng, L., Huo, H., Liu, Y. & Grey, C. P. 17O magic angle spinning NMR studies of Brønsted acid sites in zeolites HY and HZSM-5. *J. Am. Chem. Soc.* **129**, 335–346 (2007).

71. Li, S. & Deng, F. Solid-State NMR Studies of Zeolites. in *Zeolites in Sustainable Chemistry: Synthesis, Characterization and Catalytic Applications* (eds. Xiao, F.-S. & Meng, X.) 231–268 (Springer Berlin Heidelberg, 2016). doi:10.1007/978-3-662-47395-5_7.

72. Kong, X. *et al.* Mapping of Functional Groups in Metal-Organic Frameworks. *Science* **341**, 882–885 (2013).

73. Lucier, B. E. G., Chen, S. & Huang, Y. Characterization of Metal–Organic Frameworks: Unlocking the Potential of Solid-State NMR. *Acc. Chem. Res.* **51**, 319–330 (2018).

74. Brunner, E. & Rauche, M. Solid-state NMR spectroscopy: an advancing tool to analyse the structure and properties of metal–organic frameworks. *Chem. Sci.* **11**, 4297–4304 (2020).

75. Smith, B. J. *et al.* Origins of saccharide-dependent hydration at aluminate, silicate, and aluminosilicate surfaces. *Proc. Natl. Acad. Sci.* **108**, 8949–8954 (2011).

76. Kumar, A. *et al.* The Atomic-Level Structure of Cementitious Calcium Silicate Hydrate. *J. Phys. Chem. C* **121**, 17188–17196 (2017).

77. Walkley, B. & Provis, J. L. Solid-state nuclear magnetic resonance spectroscopy of cements. *Mater. Today Adv.* **1**, 100007 (2019).

78. Liu, T. *et al.* Cycling Li-O 2 batteries via LiOH formation and decomposition. *Science* **350**, 530–533 (2015).

79. Pecher, O., Carretero-González, J., Griffith, K. J. & Grey, C. P. Materials' Methods: NMR in Battery Research. *Chem. Mater.* **29**, 213–242 (2017).

80. Blanc, F., Leskes, M. & Grey, C. P. In situ solid-state NMR spectroscopy of electrochemical cells: Batteries, supercapacitors, and fuel cells. *Acc. Chem. Res.* **46**, 1952–1963 (2013).

81. Yesinowski, J. P. Solid-State NMR of Inorganic Semiconductors. in *Solid State NMR* (ed. Chan, J. C. C.) 229–312 (Springer, 2012). doi:10.1007/128_2011_208.

82. Haase, J., Curro, N. J., Stern, R. & Slichter, C. P. New Methods for NMR of Cuprate Superconductors. *Phys. Rev. Lett.* **81**, 1489–1492 (1998).

83. F. Smith, D. & P. Slichter, C. The Study of Mechanisms of Superconductivity by NMR Relaxation. in *Novel NMR and EPR techniques* (eds. Dolinšek, J., Vilfan, M. & Žumer, S.) 243–295 (Springer Berlin Heidelberg, 2006). doi:10.1007/3-540-32627-8_9.

84. Buzea, C. & Yamashita, T. Review of the superconducting properties of MgB2. *Supercond. Sci. Technol.* **14**, R115–R146 (2001).

85. Cadars, S. *et al.* Atomic Positional Versus Electronic Order in Semiconducting ZnSe Nanoparticles. *Phys. Rev. Lett.* **103**, 136802 (2009).

86. Casabianca, L. B. Solid-state nuclear magnetic resonance studies of nanoparticles. *Solid State Nucl. Magn. Reson.* **107**, 101664 (2020).

87. Anderson, W. A. & Arnold, J. T. A Line-Narrowing Experiment. *Phys. Rev.* **94**, 497–498 (1954).

88. Pines, A., Gibby, M. G. & Waugh, J. S. Proton-enhanced NMR of dilute spins in solids. *J. Chem. Phys.* 569–590 (1973) doi:10.1063/1.1680061.

89. Aue, W. P., Bartholdi, E. & Ernst, R. R. Two-dimensional spectroscopy. Application to nuclear magnetic resonance. *J. Chem. Phys.* **64**, 2229–2246 (1976).

90. Lesage, A., Bardet, M. & Emsley, L. Through-Bond Carbon−Carbon Connectivities in Disordered Solids by NMR. *J. Am. Chem. Soc.* **121**, 10987–10993 (1999).

91. Gullion, T. & Schaefer, J. Rotational-echo double-resonance NMR. *J. Magn. Reson. 1969* **81**, 196–200 (1989).

92. Rossini, A. J. *et al.* Dynamic Nuclear Polarization Surface Enhanced NMR Spectroscopy. *Acc. Chem. Res.* **46**, 1942–1951 (2013).

93. Lilly Thankamony, A. S., Wittmann, J. J., Kaushik, M. & Corzilius, B. Dynamic nuclear polarization for sensitivity enhancement in modern solid-state NMR. *Prog. Nucl. Magn. Reson. Spectrosc.* **102–103**, 120–195 (2017).

94. Lesage, A. *et al.* Surface enhanced NMR spectroscopy by dynamic nuclear polarization. *J. Am. Chem. Soc.* **132**, 15459–15461 (2010).

95. Rossini, A. J. *et al.* Dynamic nuclear polarization NMR spectroscopy of microcrystalline solids. *J. Am. Chem. Soc.* **134**, 16899–16908 (2012).

96. Björgvinsdóttir, S., Walder, B. J., Pinon, A. C. & Emsley, L. Bulk Nuclear Hyperpolarization of Inorganic Solids by Relay from the Surface. *J. Am. Chem. Soc.* **140**, 7946–7951 (2018).

97. Harris, R. K., Wasylishen, R. E. & Duer, M. J. *NMR Crystallography*. (Wiley, 2012).

98. Berruyer, P. *et al.* Three-dimensional structure determination of surface sites. *J. Am. Chem. Soc.* **139**, 849–855 (2017).

99. Grant, J. T. *et al.* Selective oxidative dehydrogenation of propane to propene using boron nitride catalysts. *Science* **354**, 1570–1573 (2016).

100. Dorn, R. W. *et al.* Structure Determination of Boron-Based Oxidative Dehydrogenation Heterogeneous Catalysts With Ultrahigh Field 35.2 T 11B Solid-State NMR Spectroscopy. *ACS Catal.* **10**, 13852–13866 (2020).

101. Dorn, R. W. *et al.* Identifying the Molecular Edge Termination of Exfoliated Hexagonal Boron Nitride Nanosheets with Solid-State NMR Spectroscopy and Plane-Wave DFT Calculations. *Chem. Mater.* **32**, 3109–3121 (2020).

102. Forse, A. C. *et al.* Elucidating CO2 Chemisorption in Diamine-Appended Metal–Organic Frameworks. *J. Am. Chem. Soc.* **140**, 18016–18031 (2018).

103. Facelli, J. C. & Grant, D. M. Determination of molecular symmetry in crystalline naphthalene using solid-state NMR. *Nature* **365**, 325–327 (1993).

104. Sebastiani, D. & Parrinello, M. A New ab-Initio Approach for NMR Chemical Shifts in Periodic Systems. *J. Phys. Chem. A* **105**, 1951–1958 (2001).

105. Ashbrook, S. E. & McKay, D. Combining solid-state NMR spectroscopy with first-principles calculations – a guide to NMR crystallography. *Chem. Commun.* **52**, 7186–7204 (2016).

106. Blöchl, P. E. Projector augmented-wave method. *Phys. Rev. B* **50**, 17953–17979 (1994).

107. Pickard, C. J. & Mauri, F. All-electron magnetic response with pseudopotentials: NMR chemical shifts. *Phys. Rev. B* **63**, 245101 (2001).

108. Yates, J. R., Pickard, C. J. & Mauri, F. Calculation of NMR chemical shifts for extended systems using ultrasoft pseudopotentials. *Phys. Rev. B* **76**, 024401 (2007).

109. Dračínský, M. & Hodgkinson, P. A molecular dynamics study of the effects of fast molecular motions on solid-state NMR parameters. *CrystEngComm* **15**, 8705–8712 (2013).

110. Cuny, J., Xie, Y., Pickard, C. J. & Hassanali, A. A. Ab Initio Quality NMR Parameters in Solid-State Materials Using a High-Dimensional Neural-Network Representation. *J. Chem. Theory Comput.* **12**, 765–773 (2016).

111. Paruzzo, F. M. *et al.* Chemical shifts in molecular solids by machine learning. *Nat. Commun.* **9**, 4501 (2018).

112. Xu, Z. & Stebbins, J. F. Cation Dynamics and Diffusion in Lithium Orthosilicate: Two-Dimensional Lithium-6 NMR. *Science* **270**, 1332–1334 (1995).

113. Verhoeven, V. W. J. *et al.* Lithium Dynamics in ${\mathrm{LiMn}}_{2}{O}_{4}$ Probed Directly by Two-Dimensional ${}^{7}\mathrm{Li}$ NMR. *Phys. Rev. Lett.* **86**, 4314–4317 (2001).

114. Moudrakovski, I. L., Ratcliffe, C. I. & Ripmeester, J. A. Application of 129 Xe 2D-EXSY NMR to intra- and interparticle exchange in zeolites. *Appl. Magn. Reson.* **8**, 385–399 (1995).

115. Schmidt-Rohr, K. *et al.* Molecular Nature of the .beta. Relaxation in Poly(methyl methacrylate) Investigated by Multidimensional NMR. *Macromolecules* **27**, 4733–4745 (1994).

116. Wasylishen, R. E., Ashbrook, S. & Wimperis, S. *NMR of Quadrupolar Nuclei in Solid Materials*. (Wiley, 2012).

117. Bureekaew, S. *et al.* One-dimensional imidazole aggregate in aluminium porous coordination polymers with high proton conductivity. *Nat. Mater.* **8**, 831–836 (2009).

118. Vukotic, V. N., Harris, K. J., Zhu, K., Schurko, R. W. & Loeb, S. J. Metal–organic frameworks with dynamic interlocked components. *Nat. Chem.* **4**, 456–460 (2012).

119. Shustova, N. B. *et al.* Phenyl Ring Dynamics in a Tetraphenylethylene-Bridged Metal–Organic Framework: Implications for the Mechanism of Aggregation-Induced Emission. *J. Am. Chem. Soc.* **134**, 15061–15070 (2012).

120. Böhmer, R., Diezemann, G., Hinze, G. & Rössler, E. Dynamics of supercooled liquids and glassy solids. *Prog. Nucl. Magn. Reson. Spectrosc.* **39**, 191–267 (2001).

121. Eckert, H. Structural characterization of noncrystalline solids and glasses using solid state NMR. *Prog. Nucl. Magn. Reson. Spectrosc.* **24**, 159–293 (1992).

122. Vinod Chandran, C. & Heitjans, P. Chapter One - Solid-State NMR Studies of Lithium Ion Dynamics Across Materials Classes. in *Annual Reports on NMR Spectroscopy* (ed. Webb, G. A.) vol. 89 1–102 (Academic Press, 2016).

123. McClelland, I. *et al.* Muon Spectroscopy for Investigating Diffusion in Energy Storage Materials. *Annu. Rev. Mater. Res.* **50**, 371–393 (2020).

124. Heitjans, P., Schirmer, A. & Indris, S. NMR and β-NMR Studies of Diffusion in Interface-Dominated and Disordered Solids. in *Diffusion in Condensed Matter: Methods, Materials, Models* (eds. Heitjans, P. & Kärger, J.) 367–415 (Springer Berlin Heidelberg, 2005). doi:10.1007/3-540-30970-5_9.

125. Zuo, L. *et al.* Polymer-modified halide perovskite films for efficient and stable planar heterojunction solar cells. *Sci. Adv.* **3**, e1700106 (2017).

126. Zhao, Y. *et al.* A polymer scaffold for self-healing perovskite solar cells. *Nat. Commun.* **7**, 10228 (2016).

127. Bi, D. *et al.* Polymer-templated nucleation and crystal growth of perovskite films for solar cells with efficiency greater than 21%. *Nat. Energy* **1**, (2016).

128. Han, T.-H. *et al.* Perovskite-polymer composite cross-linker approach for highly-stable and efficient perovskite solar cells. *Nat. Commun.* **10**, 1–10 (2019).

129. Yadav, S. K. *et al.* Metal Halide Perovskite@Metal-Organic Framework Hybrids: Synthesis, Design, Properties, and Applications. *Small* **16**, 2004891 (2020).

130. Sun, J.-Y. *et al.* Facile Two-Step Synthesis of All-Inorganic Perovskite CsPbX3 (X = Cl, Br, and I) Zeolite-Y Composite Phosphors for Potential Backlight Display Application. *Adv. Funct. Mater.* **27**, 1704371 (2017).

131. Ye, Y. *et al.* Highly Luminescent Cesium Lead Halide Perovskite Nanocrystals Stabilized in Glasses for Light-Emitting Applications. *Adv. Opt. Mater.* **7**, 1801663 (2019).

132. Bi, C., Zheng, X., Chen, B., Wei, H. & Huang, J. Spontaneous Passivation of Hybrid Perovskite by Sodium Ions from Glass Substrates: Mysterious Enhancement of Device Efficiency Revealed. *ACS Energy Lett.* **2**, 1400–1406 (2017).

133. Ahmad, S., George, C., Beesley, D. J., Baumberg, J. J. & De Volder, M. Photo-Rechargeable Organo-Halide Perovskite Batteries. *Nano Lett.* **18**, 1856–1862 (2018).

134. Kubicki, D. J., Prochowicz, D., Hofstetter, A., Walder, B. J. & Emsley, L. 113Cd Solid-State NMR at 21.1 T Reveals the Local Structure and Passivation Mechanism of Cadmium in Hybrid and All-Inorganic Halide Perovskites. *ACS Energy Lett.* **5**, 2964–2971 (2020).

135. Ruiz-Preciado, M. A. *et al.* Supramolecular Modulation of Hybrid Perovskite Solar Cells via Bifunctional Halogen Bonding Revealed by Two-Dimensional 19F Solid-State NMR Spectroscopy. *J. Am. Chem. Soc.* **142**, 1645–1654 (2020).

136. Lu, H. *et al.* Vapor-assisted deposition of highly efficient, stable black-phase FAPbI3 perovskite solar cells. *Science* **370**, (2020).

137. Van Gompel, W. T. M. *et al.* Degradation of the Formamidinium Cation and the Quantification of the Formamidinium-Methylammonium Ratio in Lead Iodide Hybrid Perovskites by Nuclear Magnetic Resonance Spectroscopy. *J. Phys. Chem. C* **122**, 4117–4124 (2018).

138. Prochowicz, D. *et al.* One-step mechanochemical incorporation of an insoluble cesium additive for high performance planar heterojunction solar cells. *Nano Energy* **49**, 523–528 (2018).

139. Kubicki, D. J. *et al.* Doping and phase segregation in Mn2+- and Co2+-doped lead halide perovskites from 133Cs and 1H NMR relaxation enhancement. *J. Mater. Chem. A* **7**, 2326–2333 (2019).

140. Nayak, P. K. *et al.* Impact of Bi3+ Heterovalent Doping in Organic–Inorganic Metal Halide Perovskite Crystals. *J. Am. Chem. Soc.* **140**, 574–577 (2018).

141. Mozur, E. M. *et al.* Cesium Substitution Disrupts Concerted Cation Dynamics in Formamidinium Hybrid Perovskites. *Chem. Mater.* (2020) doi:10.1021/acs.chemmater.0c01862.

142. García-Rodríguez, R., Ferdani, D., Pering, S., Baker, P. J. & Cameron, P. J. Influence of bromide content on iodide migration in inverted MAPb(I1−xBrx)3 perovskite solar cells. *J. Mater. Chem. A* **7**, 22604–22614 (2019).

143. Ferdani, D. W. *et al.* Partial cation substitution reduces iodide ion transport in lead iodide perovskite solar cells. *Energy Environ. Sci.* **12**, 2264–2272 (2019).

144. Senocrate, A., Moudrakovski, I. & Maier, J. Short-range ion dynamics in methylammonium lead iodide by multinuclear solid state NMR and 127I NQR. *Phys. Chem. Chem. Phys.* **20**, 20043–20055 (2018).

145. Noel, N. K. *et al.* Interfacial charge-transfer doping of metal halide perovskites for high performance photovoltaics. *Energy Environ. Sci.* (2019) doi:10.1039/C9EE01773A.

146. Nagane, S. *et al.* Tetrafluoroborate-Induced Reduction in Defect Density in Hybrid Perovskites through Halide Management. submitted.

147. Volkov, A. F., Venevtsev, Y. N. & Semin, G. K. Nuclear Quadrupole Resonance (NQR) of 79Br and 81Br in Perovskite and Orthorhombic Forms of CsPbBr3 and CsPbJ3. *Phys. Status Solidi B* **35**, K167–K169 (1969).

148. Sharma, S., Weiden, N. & Weiss, A. Phase Transitions in CsSnCl3 and CsPbBr3 An NMR and NQR Study. *Z. Für Naturforschung A* **46**, 329–336 (1991).

149. Xu, Q., Eguchi, T., Nakayama, H., Nakamura, N. & Kishita, M. Molecular Motions and Phase Transitions in Solid CH3NH3PbX3 (X = C1, Br, I) as Studied by NMR and NQR. *Z. Für Naturforschung A* **46**, 240–246 (1991).

150. Piveteau, L. *et al.* Bulk and Nanocrystalline Cesium Lead-Halide Perovskites as Seen by Halide Magnetic Resonance. *ACS Cent. Sci.* **6**, 1138–1149 (2020).

151. Johnson, R. L. & Schmidt-Rohr, K. Quantitative solid-state 13C NMR with signal enhancement by multiple cross polarization. *J. Magn. Reson.* **239**, 44–49 (2014).

152. Vinogradov, E., Madhu, P. K. & Vega, S. High-resolution proton solid-state NMR spectroscopy by phase-modulated Lee-Goldburg experiment. *Chem. Phys. Lett.* **314**, 443–450 (1999).

153. Sakellariou, D., Lesage, A., Hodgkinson, P. & Emsley, L. Homonuclear dipolar decoupling in solid-state NMR using continuous phase modulation. *Chem. Phys. Lett.* **319**, 253–260 (2000).

154. Elena, B., de Paëpe, G. & Emsley, L. Direct spectral optimisation of proton-proton homonuclear dipolar decoupling in solid-state NMR. *Chem. Phys. Lett.* **398**, 532–538 (2004).

155. Paruzzo, F. M. & Emsley, L. High-resolution 1H NMR of powdered solids by homonuclear dipolar decoupling. *J. Magn. Reson.* **309**, 106598 (2019).

156. Nishiyama, Y. Fast magic-angle sample spinning solid-state NMR at 60–100kHz for natural abundance samples. *Solid State Nucl. Magn. Reson.* **78**, 24–36 (2016).

157. Moutzouri, P., Paruzzo, F. M., Almeida, B. S. de, Stevanato, G. & Emsley, L. Homonuclear Decoupling in 1H NMR of Solids by Remote Correlation. *Angew. Chem. Int. Ed.* **59**, 6235–6238 (2020).

158. Ferrara, C. *et al.* Wide band-gap tuning in Sn-based hybrid perovskites through cation replacement: the FA1−xMAxSnBr3 mixed system. *J. Mater. Chem. A* **5**, 9391–9395 (2017).

159. Kazemi, M. A. A. *et al.* Molecular-Level Insight into Correlation between Surface Defects and Stability of Methylammonium Lead Halide Perovskite Under Controlled Humidity. *Small Methods* **5**, 2000834 (2021).

160. Xiao, M. *et al.* A Fast Deposition-Crystallization Procedure for Highly Efficient Lead Iodide Perovskite Thin-Film Solar Cells. *Angew. Chem.-Int. Ed.* **53**, 9898–9903 (2014).

161. Elena, B. & Emsley, L. Powder Crystallography by Proton Solid-State NMR Spectroscopy. *J. Am. Chem. Soc.* **127**, 9140–9146 (2005).

162. Schmidt-Rohr, K. & Spiess, H. W. *Multidimensional Solid-State NMR and Polymers - 1st Edition*. (Elsevier, 2012).

163. Krishna, A. *et al.* Defect Passivation via the Incorporation of Tetrapropylammonium Cation Leading to Stability Enhancement in Lead Halide Perovskite. *Adv. Funct. Mater.* **30**, 1909737 (2020).

164. Emsley, L. Spin Diffusion for NMR Crystallography. in *eMagRes* (Wiley, 2009). doi:10.1002/9780470034590.emrstm1010.

165. Pickard, C. J., Salager, E., Pintacuda, G., Elena, B. & Emsley, L. Resolving structures from powders by NMR crystallography using combined proton spin diffusion and plane wave DFT calculations. *J. Am. Chem. Soc.* **129**, 8932–8933 (2007).

166. Pines, A., Gibby, M. G. & Waugh, J. S. Proton-enhanced nuclear induction spectroscopy. a method for high resolution nmr of dilute spins in solids. *J. Chem. Phys.* **56**, 1776–1777 (1972).

167. Tavakoli, M. M. *et al.* Addition of adamantylammonium iodide to hole transport layers enables highly efficient and electroluminescent perovskite solar cells. *Energy Environ. Sci.* **11**, 3310–3320 (2018).

168. Saliba, M. *et al.* Cesium-containing triple cation perovskite solar cells: improved stability, reproducibility and high efficiency. *Energy Environ. Sci.* **9**, 1989–1997 (2016).

169. Li, Z. *et al.* Stabilizing Perovskite Structures by Tuning Tolerance Factor: Formation of Formamidinium and Cesium Lead Iodide Solid-State Alloys. *Chem. Mater.* **28**, 284–292 (2016).

170. Ray, A. *et al.* Green-Emitting Powders of Zero-Dimensional Cs4PbBr6: Delineating the Intricacies of the Synthesis and the Origin of Photoluminescence. *Chem. Mater.* (2019) doi:10.1021/acs.chemmater.9b02944.

171. Riesen, N., Lockrey, M., Badek, K. & Riesen, H. On the origins of the green luminescence in the "zero-dimensional perovskite" Cs4PbBr6: conclusive results from cathodoluminescence imaging. *Nanoscale* **11**, 3925–3932 (2019).

172. Yin, J. *et al.* Intrinsic Lead Ion Emissions in Zero-Dimensional Cs4PbBr6 Nanocrystals. *ACS Energy Lett.* **2**, 2805–2811 (2017).

173. Chen, Y. *et al.* Surface Termination of CsPbBr3 Perovskite Quantum Dots Determined by Solid-State NMR Spectroscopy. *J. Am. Chem. Soc.* **142**, 6117–6127 (2020).

174. Shamsi, J. *et al.* Stable Hexylphosphonate-Capped Blue-Emitting Quantum-Confined CsPbBr3 Nanoplatelets. *ACS Energy Lett.* **5**, 1900–1907 (2020).

175. Piveteau, L. *et al.* Resolving the Core and the Surface of CdSe Quantum Dots and Nanoplatelets Using Dynamic Nuclear Polarization Enhanced PASS-PIETA NMR Spectroscopy. *ACS Cent. Sci.* **4**, 1113–1125 (2018).

176. Saliba, M. *et al.* Incorporation of rubidium cations into perovskite solar cells improves photovoltaic performance. *Science* **354**, 206–209 (2016).

177. Abdi-Jalebi, M. *et al.* Maximizing and stabilizing luminescence from halide perovskites with potassium passivation. *Nature* **555**, 497 (2018).

178. Abdi-Jalebi, M. *et al.* Dedoping of Lead Halide Perovskites Incorporating Monovalent Cations. *ACS Nano* **12**, 7301–7311 (2018).

179. Fang, Z., He, H., Gan, L., Li, J. & Ye, Z. Understanding the Role of Lithium Doping in Reducing Nonradiative Loss in Lead Halide Perovskites. *Adv. Sci.* **5**, 1800736 (2018).

180. Pazoki, M., Jacobsson, T. J., Hagfeldt, A., Boschloo, G. & Edvinsson, T. Effect of metal cation replacement on the electronic structure of metalorganic halide perovskites: Replacement of lead with alkaline-earth metals. *Phys. Rev. B* **93**, 144105 (2016).

181. Bahadur, J. *et al.* Enhanced moisture stability of MAPbI3 perovskite solar cells through Barium doping. *Sol. Energy* **190**, 396–404 (2019).

182. Pérez-del-Rey, D. *et al.* Strontium Insertion in Methylammonium Lead Iodide: Long Charge Carrier Lifetime and High Fill-Factor Solar Cells. *Adv. Mater.* **28**, 9839–9845 (2016).

183. Caprioglio, P. *et al.* High open circuit voltages in pin-type perovskite solar cells through strontium addition. *Sustain. Energy Fuels* **3**, 550–563 (2019).

184. Jacobsson, T. J., Pazoki, M., Hagfeldt, A. & Edvinsson, T. Goldschmidt's Rules and Strontium Replacement in Lead Halogen Perovskite Solar Cells: Theory and Preliminary Experiments on CH3NH3SrI3. *J. Phys. Chem. C* **119**, 25673–25683 (2015).

185. Phung, N. *et al.* The Doping Mechanism of Halide Perovskite Unveiled by Alkaline Earth Metals. *J. Am. Chem. Soc.* **142**, 2364–2374 (2020).

186. Lu, C. *et al.* Calcium doped MAPbI3 with better energy state alignment in perovskite solar cells. *Appl. Phys. Lett.* **112**, 193901 (2018).

187. Yang, F. *et al.* Magnesium-Doped MAPbI3 Perovskite Layers for Enhanced Photovoltaic Performance in Humid Air Atmosphere. *ACS Appl. Mater. Interfaces* **10**, 24543–24548 (2018).

188. Huang, Q. *et al.* Suppressing defect states in CsPbBr3 perovskite via magnesium substitution for efficient all-inorganic light-emitting diodes. *Nanoscale Horiz.* **4**, 924–932 (2019).

189. Park, B. *et al.* Chemical engineering of methylammonium lead iodide/bromide perovskites: tuning of opto-electronic properties and photovoltaic performance. *J. Mater. Chem. A* **3**, 21760–21771 (2015).

190. Hu, Y., Aygueler, M. F., Petrus, M. L., Bein, T. & Docampo, Pablo. Impact of Rubidium and Cesium Cations on the Moisture Stability of Multiple-Cation Mixed-Halide Perovskites. *ACS Energy Lett.* **2**, 2212–2218 (2017).

191. Kanwat, A. *et al.* Stabilizing the Electroluminescence of Halide Perovskites with Potassium Passivation. *ACS Energy Lett.* **5**, 1804–1813 (2020).

192. Sharenko, A., Mackeen, C., Jewell, L., Bridges, F. & Toney, M. F. Evolution of Iodoplumbate Complexes in Methylammonium Lead Iodide Perovskite Precursor Solutions. *Chem. Mater.* **29**, 1315–1320 (2017).

193. Radicchi, E., Mosconi, E., Elisei, F., Nunzi, F. & De Angelis, F. Understanding the Solution Chemistry of Lead Halide Perovskites Precursors. *ACS Appl. Energy Mater.* **2**, 3400–3409 (2019).

194. Navas, J. *et al.* Revealing the role of Pb2+ in the stability of organic–inorganic hybrid perovskite CH3NH3Pb1−xCdxI3: an experimental and theoretical study. *Phys. Chem. Chem. Phys.* **17**, 23886–23896 (2015).

195. Dunlap-Shohl, W. A., Younts, R., Gautam, B., Gundogdu, K. & Mitzi, D. B. Effects of Cd Diffusion and Doping in High-Performance Perovskite Solar Cells Using CdS as Electron Transport Layer. *J. Phys. Chem. C* **120**, 16437–16445 (2016).

196. van der Stam, W. *et al.* Highly Emissive Divalent-Ion-Doped Colloidal CsPb1-xMxBr3 Perovskite Nanocrystals through Cation Exchange. *J. Am. Chem. Soc.* **139**, 4087–4097 (2017).

197. Saidaminov, M. I. *et al.* Suppression of atomic vacancies via incorporation of isovalent small ions to increase the stability of halide perovskite solar cells in ambient air. *Nat. Energy* **3**, 648–654 (2018).

198. Parobek, D. *et al.* Exciton-to-Dopant Energy Transfer in Mn-Doped Cesium Lead Halide Perovskite Nanocrystals. *Nano Lett.* **16**, 7376–7380 (2016).

199. Zou, S. *et al.* Stabilizing Cesium Lead Halide Perovskite Lattice through Mn(II) Substitution for Air-Stable Light-Emitting Diodes. *J. Am. Chem. Soc.* **139**, 11443–11450 (2017).

200. Xu, K., Lin, C. C., Xie, X. & Meijerink, Andries. Efficient and Stable Luminescence from Mn2+ in Core and Core-Isocrystalline Shell CsPbCl3 Perovskite Nanocrystals. *Chem. Mater.* **29**, 4265–4272 (2017).

201. Mir, W. J., Jagadeeswararao, M., Das, S. & Nag, Angshuman. Colloidal Mn-Doped Cesium Lead Halide Perovskite Nanoplatelets. *ACS Energy Lett.* **2**, 537–543 (2017).

202. Yao, J.-S. *et al.* Ce3+-Doping to Modulate Photoluminescence Kinetics for Efficient CsPbBr3 Nanocrystals Based Light-Emitting Diodes. *J. Am. Chem. Soc.* **140**, 3626–3634 (2018).

203. Pell, A. J., Pintacuda, G. & Grey, C. P. Paramagnetic NMR in solution and the solid state. *Prog. Nucl. Magn. Reson. Spectrosc.* (2018) doi:10.1016/j.pnmrs.2018.05.001.

204. Klug, M. T. *et al.* Tailoring metal halide perovskites through metal substitution: influence on photovoltaic and material properties. *Energy Environ. Sci.* **10**, 236–246 (2017).

205. Shmyreva, A. A., Safdari, M., Furó, I. & Dvinskikh, S. V. NMR longitudinal relaxation enhancement in metal halides by heteronuclear polarization exchange during magic-angle spinning. *J. Chem. Phys.* **144**, 224201 (2016).

206. Bernard, G. M. *et al.* Methylammonium lead chloride: A sensitive sample for an accurate NMR thermometer. *J. Magn. Reson.* **283**, 14–21 (2017).

207. Aebli, M. *et al.* Lead-Halide Scalar Couplings in 207 Pb NMR of APbX 3 Perovskites (A = Cs, Methylammonium, Formamidinium; X = Cl, Br, I). *Sci. Rep.* **10**, 8229 (2020).

208. Kubicki, D. J. *et al.* Amplifying Dynamic Nuclear Polarization of Frozen Solutions by Incorporating Dielectric Particles. *J. Am. Chem. Soc.* **136**, 15711–15718 (2014).

209. Walder, B. J. *et al.* One- and Two-Dimensional High-Resolution NMR from Flat Surfaces. *ACS Cent. Sci.* **5**, 515–523 (2019).

210. Fabini, D. H. *et al.* Dynamic Stereochemical Activity of the Sn2+ Lone Pair in Perovskite CsSnBr3. *J. Am. Chem. Soc.* **138**, 11820–11832 (2016).

211. Fabini, D. H., Seshadri, R. & Kanatzidis, M. G. The underappreciated lone pair in halide perovskites underpins their unusual properties. *MRS Bull.* **45**, 467–477 (2020).

212. Laurita, G., H. Fabini, D., C. Stoumpos, C., G. Kanatzidis, M. & Seshadri, R. Chemical tuning of dynamic cation off-centering in the cubic phases of hybrid tin and lead halide perovskites. *Chem. Sci.* **8**, 5628–5635 (2017).

213. Yamada, K., Fujise, K., Hino, S., Yamane, Y. & Nakagama, T. Characterization of Sn(II)-based Perovskites by XRD, DTA, NQR and 119Sn NMR for Photovoltaic Applications. *Chem. Lett.* **48**, 749–752 (2019).

214. Ha, M. *et al.* Phase Evolution in Methylammonium Tin Halide Perovskites with Variable Temperature Solid-State 119Sn NMR Spectroscopy. *J. Phys. Chem. C* **124**, 15015–15027 (2020).

215. Chung, I. *et al.* CsSnI3: Semiconductor or Metal? High Electrical Conductivity and Strong Near-Infrared Photoluminescence from a Single Material. High Hole Mobility and Phase-Transitions. *J. Am. Chem. Soc.* **134**, 8579–8587 (2012).

216. Karmakar, A., Bhattacharya, A., Bernard, G. M., Mar, A. & Michaelis, V. K. Revealing the Local Sn and Pb Arrangements in CsSnxPb1–xBr3 Perovskites with Solid-State NMR Spectroscopy. *ACS Mater. Lett.* 261–267 (2021) doi:10.1021/acsmaterialslett.0c00596.

217. Kubicki, D. J. *et al.* Halide Mixing and Phase Segregation in Cs2AgBiX6 (X = Cl, Br, and I) Double Perovskites from Cesium-133 Solid-State NMR and Optical Spectroscopy. *Chem. Mater.* **32**, 8129–8138 (2020).

218. O'Dell, L. A. & Schurko, R. W. Static solid-state 14N NMR and computational studies of nitrogen EFG tensors in some crystalline amino acids. *Phys. Chem. Chem. Phys.* **11**, 7069–7077 (2009).

219. O'Dell, L. A., Schurko, R. W., Harris, K. J., Autschbach, J. & Ratcliffe, C. I. Interaction Tensors and Local Dynamics in Common Structural Motifs of Nitrogen: A Solid-State 14N NMR and DFT Study. *J. Am. Chem. Soc.* **133**, 527–546 (2011).

220. Schurko, R. W. Ultra-Wideline Solid-State NMR Spectroscopy. *Acc. Chem. Res.* **46**, 1985–1995 (2013).

221. Wasylishen, R. E., Pettitt, B. A. & Jeffrey, K. R. NMR investigation of orientationally disordered NaCN and KCN. *J. Chem. Phys.* **74**, 6022–6026 (1981).

222. O'Reilly, D. E., Peterson, E. M., Scheie, C. E. & Kadaba, P. K. Nitrogen-14 and sodium-23 nuclear magnetic resonance of sodium and potassium cyanide. *J. Chem. Phys.* **58**, 3018–3022 (1973).

223. Fabini, D. H. *et al.* Reentrant Structural and Optical Properties and Large Positive Thermal Expansion in Perovskite Formamidinium Lead Iodide. *Angew. Chem. Int. Ed.* **55**, 15392–15396 (2016).

224. Ghosh, D., Walsh Atkins, P., Islam, M. S., Walker, A. B. & Eames, C. Good Vibrations: Locking of Octahedral Tilting in Mixed-Cation Iodide Perovskites for Solar Cells. *ACS Energy Lett.* **2**, 2424–2429 (2017).

225. Spiess, H. W. Molecular dynamics of solid polymers as revealed by deuteron NMR. *Colloid Polym. Sci.* **261**, 193–209 (1983).

226. Brown, S. P. & Spiess, H. W. Advanced Solid-State NMR Methods for the Elucidation of Structure and Dynamics of Molecular, Macromolecular, and Supramolecular Systems. *Chem. Rev.* **101**, 4125–4156 (2001).

227. Qiao, W.-C. *et al.* Metastable alloying structures in MAPbI 3−x Cl x crystals. *NPG Asia Mater.* **12**, 1–10 (2020).

228. Fabini, D. H. *et al.* Main-Group Halide Semiconductors Derived from Perovskite: Distinguishing Chemical, Structural, and Electronic Aspects. *Inorg. Chem.* **56**, 11–25 (2017).

229. Lipari, G. & Szabo, A. Model-Free Approach to the Interpretation of Nuclear Magnetic Resonance Relaxation in Macromolecules. 1. Theory and Range of Validity. *J. Am. Chem. Soc.* **104**, 4546–4559 (1982).

230. Torchia, D. A. & Szabo, Attila. Spin-lattice relaxation in solids. *J. Magn. Reson. 1969-1992* **49**, 107–21 (1982).

231. Lee, M. M., Teuscher, J., Miyasaka, T., Murakami, T. N. & Snaith, H. J. Efficient hybrid solar cells based on meso-superstructured organometal halide perovskites. *Science* **338**, 643–7 (2012).